Empa
Materials Science and Technology

Contract-N°: 16.0060.PJ/P324-0982

Quantification of Swiss Nitrous Oxide Emissions Through Atmospheric Observations and Inverse Modelling

Final Report

2019-02-21

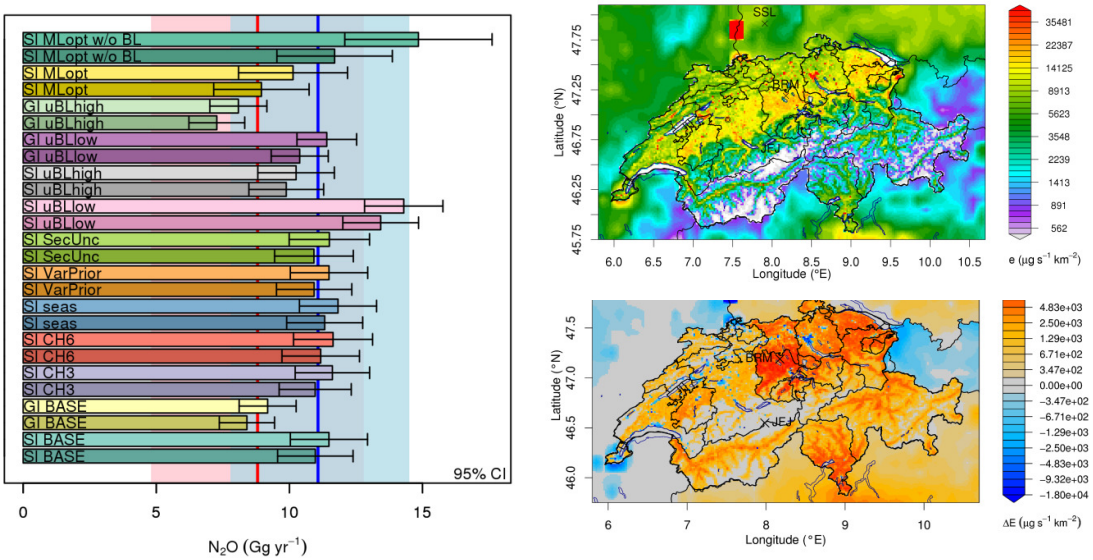

(left) Swiss total annual N_2O emissions from all sensitivity inversions, vertical lines and shading represent a priori (red) and mean a posteriori (blue); (right top) mean a priori and (right bottom) a posteriori minus a priori emissions distribution.

Laboratory for Air Pollution / Environmental Technology, Empa, 8600 Dübendorf

Stephan Henne, Joachim Mohn, Dominik Brunner,
Lukas Emmenegger

Project on behalf of Federal Office for the Environment (FOEN)

German title: Quantifizierung der Schweizer Lachgasemissionen mittels atmosphärischer Messungen und inverser Modellierung

Imprint

Project partner:

FOEN (Federal Office for the Environment), CH-3003 Bern

The Federal Office for the Environment is the Swiss environmental agency, a division of the Federal Department of Environment, Transport, Energy and Communications (DETEC).

Empa (Eidgenössische Materialprüfungs- und Forschungsanstalt), Laboratory for Air Pollution and Environmental Technology, CH-8600 Dübendorf

Authors (Empa):

Stephan Henne, Joachim Mohn, Dominik Brunner, Lukas Emmenegger

Support group for report (FOEN):

Regine Röthlisberger, Division Climate

Disclaimer:

This study was conducted by Empa in collaboration with the support group at FOEN. The respective authors are responsible for the content of this report. This study/this report was financially supported by FOEN.

Dübendorf, February 2019

Project leader	Head of laboratory
Dr. D. Brunner	Dr. L. Emmenegger

Summary **4**

Zusammenfassung **6**

1 State of research and aims of project **8**

2 Methods **10**

2.1 Establishment of continuous nitrous oxide measurements at Beromünster tall tower 10

2.1.1 Chosen analyser and laboratory tests 10

2.1.2 Field deployment 12

2.1.3 In-field performance 13

2.1.4 Data processing and baseline estimation 14

2.2 Additional nitrous oxide measurements in Switzerland and southern Germany 14

2.3 Spatially resolved emission inventory and preparation of a priori emissions 15

2.4 Atmospheric transport simulations 19

2.5 Inversion frameworks 21

2.5.1 Sectorial resolved inversion (sector inversion) 22

2.5.2 Parameters describing covariance structures 23

2.6 Setup of sensitivity inversions 23

3 Explorative data analysis for measurements at Beromünster **24**

4 Estimation of Swiss nitrous oxide emissions by inverse modelling **27**

4.1 SI_BASE inversion results 27

4.2 Sensitivity inversions 33

4.2.1 Gridded inversion 33

4.2.2 Influence of region definitions 34

4.2.3 Influence of temporal resolution of emissions 35

4.2.4 Influence of a priori time profile 36

4.2.5 Influence of a priori uncertainty by sector 37

4.2.6 Influence of baseline uncertainty 38

4.2.7 Maximum likelihood optimisation of covariance parameters 41

4.2.8 Influence of large point sources 43

4.3 Summary of sensitivity inversions 43

4.4 Relationship between nitrous oxide emissions and environmental controls 46

4.5 Discussion of previous top-down estimates of N_2O emissions in Europe 49

5 Summary and conclusions **49**

6 Outlook **50**

Acknowledgements **52**

References **53**

Glossary **55**

Summary

Nitrous oxide (N_2O) is a potent greenhouse gas and responsible for ozone destruction in the stratosphere. As such, N_2O emissions are targeted by the Kyoto Protocol and the Paris agreement and have to be included in national inventory reporting to the UNFCCC. In Switzerland, total N_2O emissions contribute about 5.6 % to national anthropogenic greenhouse gas emissions in 2016 (FOEN, 2018). These "bottom-up" estimates for N_2O are associated with large uncertainties due to the heterogeneous character of the main emission processes, i.e. direct and indirect emissions from agricultural and (semi-)natural ecosystems.

In the present project, an attempt was made to support the current bottom-up estimates as reported in the National Inventory Report (NIR) by independent estimates on the country-scale in a top-down fashion through atmospheric observations and inverse modelling, similar to previous estimates of Swiss methane (CH_4) emissions. In contrast to CH_4, the required observations and inverse modelling tools had to be set up and refined for the challenges posed by the nature of spatially and temporally variable N_2O emissions.

As part of the project, new N_2O observations were established in March 2017 at the tall tower Beromünster on the central Swiss Plateau. The performance of a newly acquired N_2O analyser (Picarro Inc.) proved to be reliable and sufficiently accurate to use these observations in inverse modelling. Here, the first 14 months of observations (March 2017 to April 2018) were analysed and, together with N_2O observations from the more remote sites Jungfraujoch and Schauinsland, were used in an atmospheric inversion of Swiss emissions. Another prerequisite for the inverse modelling was the compilation of a spatially resolved N_2O emission inventory for Switzerland. The inventory was prepared by Meteotest and includes spatially resolved (500 m x 500 m) emissions for 26 separate sectors (Meteotest, 2017).

With these atmospheric observations and a priori information, it was possible to estimate Swiss N_2O emissions at the country scale for the first time with independent methods. The best estimate of annual N_2O emissions for the investigated period in 2017/2018 was 10.9±3.4 Gg yr^{-1}, which compares to 8.7±3.5 Gg yr^{-1} given in the Swiss NIR (2-σ confidence level) (FOEN, 2018). Due to the large uncertainties connected to both numbers, these estimates are not significantly different. The relative uncertainty of the inverse modelling estimate (31 %) was somewhat smaller than that of the NIR estimate (40 %). The relatively large uncertainty range of the inverse method was calculated from the spread of 26 sensitivity inversions. These sensitivity tests comprised, but were not limited to, the application of two different inversion approaches: one focussing on the spatial distribution (grid inversion), the other on the temporal evolution and emissions by sector (sector inversion). The largest contributors to the a posteriori spread were the definition and uncertainty of a baseline of the atmospheric concentrations required by the model approach and systematic differences between grid and sector inversion.

Most of the larger emissions estimates of the inversion model as compared with the a priori estimates were assigned to direct emissions from agricultural soils (central and eastern Swiss Plateau) and to a smaller degree to indirect emissions from (semi-)natural ecosystems (southern Switzerland) and agricultural soils (northern Switzerland). The general increase from agricultural lands and (semi-)natural ecosystems may partly be explained by solely natural N_2O emissions, which were not taken into account in the applied a priori inventory, since they are not part of the NIR. Lower than a priori emissions were assigned to other types of anthropogenic emission sectors such as transport, heating, and wastewater treatment. However, the changes in these smaller sectors were associated with larger uncertainties and considerable negative covariance towards the major emission sectors. Hence, it cannot be concluded that they are significant. Some further support for this result is provided by the grid inversion, which also estimated that emissions in urban areas are potentially overestimated in the NIR.

All inversions suggested a pronounced seasonality in the emissions with a mean amplitude over all inversions of ±40 % of the annual total. Largest emissions were estimated in summer, smallest in winter. However, there was considerable spread in the seasonal amplitude as well, with the tendency of inversions with smaller annual total emissions to predict smaller summertime emissions and correspondingly smaller seasonal amplitudes. Seasonality was dominated by emissions from soils. The

month-to-month variability in soil emissions was clearly linked to two environmental controls, soil temperature and soil water filled pore space, explaining 86 % of the observed variability.

The tendency to larger than reported N_2O emissions obtained here for Switzerland compares well with other recent inverse estimates of N_2O emissions in Europe. Some of these studies also highlight a similarly pronounced seasonality.

Despite the challenges inherent to inverse estimation of N_2O emissions, this study proves that it is in general possible to retrieve them on the scale of a small country and with monthly resolution, provided adequate atmospheric observations, high resolution transport simulations, and appropriate inverse modelling tools are available.

Zusammenfassung

Distickstoffmonoxid (N_2O), besser bekannt unter dem Trivialnamen Lachgas, ist ein sehr wirksames Treibhausgas und teilweise für Ozonabbau in der Stratosphäre verantwortlich. Als solches wurde es als eines der Zielgase in internationalen Klimaverträgen (Kyoto Protokoll und Vereinbarung von Paris) aufgenommen, und seine Emissionen müssen von den Unterzeichnerstaaten jährlich im Rahmen des nationalen Emissionsberichts an das UNFCCC rapportiert werden. In der Schweiz tragen die durch menschliche Aktivitäten verursachten (anthropogenen) Emissionen von N_2O 5.6 % zu den totalen, anthropogenen Emissionen aller Treibhausgase bei (FOEN, 2018). Die Berechnung dieser Emissionen erfolgt über einen "bottom-up" Ansatz, der im Fall von N_2O und aufgrund der heterogenen Quellprozesse (direkte und indirekte Emissionen aus landwirtschaftlichen Böden und (halb-)natürlichen Ökosystemen) mit relativ grossen Unsicherheiten behaftet ist.

In der vorliegenden Studie sollte der Versuch unternommen werden, die bestehenden bottom-up Abschätzungen, wie sie im nationalen Inventarbericht (NIR) rapportiert werden, mithilfe von unabhängigen "top-down" Methoden (atmosphärische Beobachtungen und inverse Modellierung) zu unterstützen. Dies wurde zuvor schon erfolgreich für Schweizer Methanemissionen durchgeführt. Im Gegensatz zu Methan (CH_4) mussten bestehende Modellierungsmethoden weiter-, bzw. neu entwickelt werden, um der zeitlich und räumlich variablen Natur der N_2O Quellen Rechnung zu tragen. Ausserdem mussten adäquate N_2O-Messungen im Schweizer Mittelland aufgebaut werden.

Kontinuierliche N_2O-Messungen wurden als Teil dieses Projekts ab März 2017 am Sendeturm Beromünster im zentralen Schweizer Mittelland etabliert. Die Eigenschaften eines eigens für dieses Projekt neu angeschafften N_2O-Analysators (Picarro Inc.) erwiesen sich als zuverlässig und ausreichend genau, um dessen Messungen in der inversen Modellierung zu verwenden. In diesem Bericht werden die ersten 14 Monate (März 2017 bis April 2018) dieser Messungen beschrieben und mit weiteren N_2O Messungen der höher gelegenen Messstellen Jungfraujoch (Berner Oberland) und Schauinsland (Schwarzwald), sowie atmosphärischen Transportsimulationen verknüpft, um Schweizer N_2O Emissionen zu bestimmen. Eine weitere Voraussetzung für die inverse Modellierung war das Erstellen eines räumlich hoch-aufgelösten a priori Emissionsinventars für die Schweiz. Ein solches Inventar wurde von Meteotest für eine horizontale Auflösung von 500 m x 500 m erstellt und umfasst 26 separate Emissionssektoren (Meteotest, 2017).

Mit diesen neuen Messungen und Emissionsinventar als a priori Information war es erstmals mögliche, die Schweizer N_2O Emissionen für die Schweiz mit einer unabhängigen inversen Modellierungsmethode zu bestimmen. Als besten Wert aus der inversen Modellierung wurden mittlere Schweizer Emissionen von 10.9 ± 3.4 Gg yr^{-1} für den Untersuchungszeitraum 2017/2018 bestimmt. Diese können mit dem im Schweizer NIR rapportierten Wert von 8.7 ± 3.5 Gg yr^{-1} (2-σ Vertrauensintervall) verglichen werden (FOEN, 2018). Wegen der relativ grossen Unsicherheiten beider Methoden/Werte können diese nicht als signifikant unterschiedlich angesehen werden. Die relative Unsicherheit, die aus der inversen Modellierung ermittelt wurde (31 %), lag dabei etwas unter derjenigen des NIR (40 %). Die relative grosse Unsicherheit der inversen Modellierung resultiert aus der Verwendung von 26 Sensitivitätsinversion und deren Streuung. Mit diesen Sensitivitätsinversionen wurden diverse Aspekte der strukturellen Unsicherheit der inversen Methodik untersucht. Diese Aspekte umfassten unter anderem zwei grundsätzlich verschiedene Herangehensweisen der Inversion: die erste zielte auf die Optimierung des zeitlichen Emissionsverlaufs in Subregionen und Emissionssektoren ab (Sektorinversion), während die zweite auf die räumlichen Verteilung der Emissionen fokussierte (Gitterinversion). Weiterhin trugen die Definition und a priori Unsicherheit der Konzentrationsbasislinie zur relativ grossen a posteriori Unsicherheit bei.

Als Ergebnis der Sektorinversion wurden die grössten positiven Abweichungen zwischen a priori und a posteriori den direkten Emissionen von landwirtschaftlichen Flächen zugeschrieben. (zentrales und östliches Mittelland) und zu einem kleineren Anteil indirekten Emissionen aus (halb-)natürlichen Ökosystemen (Südschweiz) und indirekten Emissionen von landwirtschaftlichen Flächen (Nordschweiz). Dieser grundsätzliche Emissionsanstieg von sowohl landwirtschaftlichen als auch (halb-)natürlichen Ökosystemen könnte teilweise damit erklärt werden, dass von diesen Flächen auch natürliche Emissionen stammen könnten, die im NIR und auch dem a priori Inventar nicht erfasst sind. Emissionen aus

allen anderen anthropogenen Emissionssektoren, wie zum Beispiel Verkehr, Heizungen und Abwasserreinigungsanlagen, wurden von der inversen Methodik geringer geschätzt als im a priori Inventar. Einerseits waren diese Emissionsänderungen in den kleineren Emissionssektoren mit grösseren Unsicherheiten behaftet als die in den Hauptsektoren. Daher kann an dieser Stelle nicht von einem signifikanten Unterschied ausgegangen werden. Andererseits wurden auch von der Gitterpunktsinversion tiefere a posteriori Emissionen in mehrheitlich urbanen Regionen festgestellt, was ein weiterer Hinweis dafür sein könnte, dass die genannten Emissionsquellen im NIR überschätzt werden.

In allen durchgeführten Sensitivitätsinversionen konnte eine ausgeprägte Saisonabhängigkeit der Emissionen festgestellt werden, deren mittlere Amplitude ca. ±40 % vom Jahresmittel entspricht. Die höchsten Emissionen wurden dabei für den Sommer bestimmt, die geringsten für den Winter. Allerdings konnte auch eine deutliche Streuung in der Saisonabhängigkeit zwischen den Sensitivitätsinversionen beobachtet werden. Dabei zeigte sich, dass die Inversionen mit kleinerem Jahresmittel dieses vor allem aufgrund geringer Sommeremissionen und daher auch reduzierter jährlicher Amplitude aufwiesen. Grundsätzlich wurde die Saisonabhängigkeit von Emissionen aus Böden dominiert. Die monatliche Variabilität der Bodenemissionen konnte klar mit Umwelteinflüssen (Bodentemperatur und -feuchte) verknüpft werden, welche zusammen 86 % der beobachteten Variabilität erklären konnten.

Die hier für die Schweiz beobachtete Tendenz zu leicht höheren Emissionen aus inverser Modellierung im Vergleich zu rapportierten, anthropogenen Emissionen, konnte auch in anderen vergleichbaren Studien im Europäischen Raum festgestellt werden. Diese Studien zeigten ebenfalls eine ähnlich stark ausgeprägte saisonale Variabilität der N_2O Emissionen.

Trotz der Herausforderungen bei der inversen Bestimmung von N_2O Emissionen konnte diese Studie aufzeigen, dass es möglich ist, diese Emissionen auf der Skala eines kleinen Landes wie der Schweiz und mit monatlicher Auflösung erfolgreich zu bestimmen. Voraussetzung bleiben allerdings adäquate atmosphärische Messungen, hoch auflösende Transportsimulationen und geeignete Inversionssysteme.

1 State of research and aims of project

The average atmospheric concentration of nitrous oxide (N_2O) has increased since pre-industrial times from around 270 nmol mol^{-1} to more than 324 nmol mol^{-1} (Myhre et al., 2013). This increase resulted in an additional global average radiative forcing of 0.17 W m^{-2} in the year 2011, which represents about 10 % of the additional radiative forcing of carbon dioxide (CO_2, 1.82 W m^{-2}) (Myhre et al., 2013). Hence, nitrous oxide currently is the third most important anthropogenic greenhouse gas (GHG), after CO_2 and methane (CH_4). In addition, N_2O enhances destruction of stratospheric ozone (O_3) and is the substance with strongest impact on the ozone layer in the 21st century (Ravishankara et al., 2009). The anthropogenic contribution to the total global N_2O emissions (~12 Tg yr^{-1}) was estimated to be in the order of 30 % to 45 %, mainly originating from enhanced microbial production in fertilised agricultural soils, whereas natural emissions occur from soils under natural vegetation (~10.4 Tg yr^{-1}), oceans (~6 Tg yr^{-1}) and atmospheric chemistry (0.9 Tg yr^{-1}) (Myhre et al., 2013; Reay et al., 2012).

In Switzerland, total N_2O emissions were estimated to be 2'601 Gg CO_2-eq. yr^{-1} or 8.73 Gg N_2O yr^{-1} for the year 2016, including emissions from land use, land use change and forestry (LULUCF, 0.17 Gg N_2O yr^{-1}) and indirect N_2O emissions, which are induced by the atmospheric deposition of nitrates and ammonia (0.84 Gg N_2O yr^{-1}). Hence, N_2O emissions contributed about 5.6 % to the national anthropogenic greenhouse gas emissions (FOEN, 2018). In comparison to 1990, Swiss N_2O emissions in 2016 were reduced by 22 %, mainly due to reductions in the use of mineral fertilisers. Agriculture is the largest source sector by far, with annual emissions of 6.168 Gg yr^{-1} or 71 % of the national total. Other important source sectors are emissions from (semi-)natural ecosystems (9.6 %), fossil fuel combustion (0.755 Gg yr^{-1}, 8.6 %), waste treatment (0.644 Gg yr^{-1}, 7.4 %), and industrial processes (0.151 Gg yr^{-1}, 1.7 %).

Compared to CH_4 and especially CO_2, N_2O emission estimates from bottom-up inventories are associated with larger uncertainties. The current level of understanding of microbial source processes in soils but also in water treatment facilities is limited and subject to very large local variations based on soil properties, management practices, and environmental controls (Butterbach-Bahl et al., 2013; Daelman et al., 2015). The uncertainty estimate for total Swiss N_2O emissions for the year 2014 was 39.5 %, as compared with 18 % and 0.73 % for CH_4 and CO_2, respectively (FOEN, 2016). These large uncertainties in the calculation of bottom-up N_2O emissions are also reflected in the impact of methodological changes in the Swiss reporting between 2014 and 2015, which resulted in a downward correction of N_2O emissions by 20 %. Despite the relatively small contribution of N_2O emissions to the total GHG emission budget, these uncertainties underline the importance of an independent validation of the bottom-up estimates.

Atmospheric inverse modelling offers such an independent support and validation tool and, therefore, has gained considerable importance and has seen widespread applications in the atmospheric science community in the last three decades. It combines atmospheric composition observations in a "top-down" manner with atmospheric transport models to estimate the emissions that best fit the observations. Atmospheric transport models provide the quantitative link between temporally and spatially variable emissions and the observed temporal evolution of atmospheric concentrations (source-receptor relationship or source sensitivities). The mathematical inversion algorithm itself carries out the optimisation of emissions taking into account the source sensitivities, the observations and possible additional constraints (e.g., a priori information on emissions).

First inverse modeling studies were carried out at the global scale with coarsely resolved atmospheric transport models, allowing the estimation of hemispheric to continental scale emission fluxes. In recent years and through the availability of new observational time series and finer-scale transport models, inverse modeling on the regional scale has gained importance (Bergamaschi et al., 2018). Among the first studies providing emission estimates on the country level in support of the national UNFCCC reporting Henne et al. (2016) presented an inverse estimation of Swiss CH_4 emissions for the year 2013, which was subsequently extended to cover a longer period 2013-2016 (Henne et al., 2017). Both studies showed a close agreement (within uncertainties margins) between the national inventory reporting (NIR) and the top-down estimates in terms of total Swiss CH_4 emissions and showed a considerable reduction in a posteriori uncertainties. Furthermore, the studies provided trust in the applica-

bility of inverse modelling on the Swiss scale, despite the complex topography and heterogenic landscape encountered in Switzerland.

In the present study the existing inverse modelling framework for CH_4 was applied and extended for the estimation of Swiss N_2O emissions. In comparison to CH_4, the inverse modelling of N_2O emissions has to overcome several additional challenges. On the one hand there are only a few studies that have tried to inversely estimate N_2O emissions on the regional scale (Bergamaschi et al., 2015; Ganesan et al., 2015) and none had the resolution required to estimate emissions on the scale of a small country like Switzerland (order of 40'000 km^2). On the other hand, there were no continuous N_2O observations available from any measurement site on the Swiss Plateau at the start of the project. Only the WMO Global Atmosphere Watch (GAW) sites Jungfraujoch, Empa, and Schauinsland, Germany UBA, provided continuous observations of N_2O. However, these sites are known to lack sufficient, year-round sensitivity towards emissions on the Swiss Plateau.

Another challenge is the fact that due to its long atmospheric lifetime (~121 years in comparison with ~9 years for CH_4), the variability of N_2O mole fractions above the baseline are very small. This requires highly accurate measurements but also poses a challenge for the inverse modelling, where excursions from the baseline concentration are of importance. Furthermore, there was only limited knowledge on the spatial distribution of N_2O emissions available within Switzerland, as no national, spatially resolved inventory existed. Gridded information was only available for indirect emissions from (semi-)natural ecosystems (Bühlmann et al., 2015). Without a sufficiently well resolved a priori inventory, inverse model estimates are more uncertain since the spatial distribution of emissions puts an important additional constraint on the final solution. Finally, the character of N_2O emissions from soils (the largest contributor) poses difficulties in itself. These emissions can be expected to be temporally and spatially very variable as they may depend on many internal and external drivers such as soil properties, atmospheric drivers (temperature, precipitation) and management practices (timing and procedure of fertiliser application). Hence, N_2O emissions cannot be assumed to be constant or only slowly varying in time, as this can be done for CH_4 emissions.

Therefore, the aims of this project were threefold

1) Installation, operation, calibration of a continuous N_2O analyser at a measurement site on the Swiss Plateau. According to the experiences gained during the previous studies on CH_4, the Beromünster tall tower offers an excellent site for such measurement as its elevated inlet (212 m above ground) limits the influence of local emissions on the observations. This is desirable for model integration since small-scale and near surface effects are challenging for any atmospheric transport model. Furthermore, the location of the site provides source sensitivities for most parts of the Swiss Plateau and, therefore, covers most of the regions where large N_2O emissions were expected.
2) Preparation of a national, spatially-resolved N_2O emission inventory for different emission sectors. The inventory should be based on national total emission estimates as provided by the NIR
3) Inverse estimation of national total N_2O emissions by applying the existing atmospheric transport model for the sites Beromünster, Jungfraujoch and Schauinsland. The inversion framework must extend the framework developed previously for CH_4 in order to cope with the challenges explained above. Especially a new sectorial inversion approach should be implemented that provides limited optimization of emissions in space, but rather focusses on the optimization in time and by emission sector.

This report covers these subjects as follows: section 2 describes the automation, laboratory testing and field application of a new N_2O analyser at the Beromünster tall tower site. Furthermore, the main features of the newly derived spatially resolved N_2O emission inventory are summarized and features of the atmospheric transport model, the inversion system and its setup are discussed. Section 3 provides a brief discussion of the first complete year of N_2O observations at Beromünster. Finally, section 4 presents results of the inverse modelling of Swiss N_2O emissions. A discussion of the inverse modelling results, some conclusions and an outlook are provided in sections 5 and 6.

2 Methods

2.1 Establishment of continuous nitrous oxide measurements at Beromünster tall tower

To carry out the N_2O observations on the Swiss Plateau, a new N_2O analyser was purchased for the use in this project. The chosen analyser was a cavity ring down spectrometer (CRDS) from Piccaro Inc. (G5310). Since this analyser was new on the market, and its technology (MIR QC laser source) not used in earlier Picarro instruments, no experience in its setup, operation and maintenance were available at Empa. Therefore, the instrument was subjected to a series of thorough laboratory tests before field deployment. Furthermore, new calibration gases had to be prepared to assure the high quality of the measurements and the inter-comparability with other observations. Finally, a sample switch unit had to be designed, built and integrated into the existing sampling system at the Beromünster tall tower site.

2.1.1 Chosen analyser and laboratory tests

After an evaluation of N_2O analysers commercially available, Picarro Inc.: G5310 (N_2O, CO, H_2O), G5131-i (N_2O, $\delta^{15}N^{\alpha}$, $\delta^{15}N^{\beta}$, $\delta^{18}O$), Los Gatos Research Inc.: 931-0015 enhanced performance (N_2O, CO, H_2O) and Aerodyne Inc.: cw QC-TILDAS-76-CS (N_2O, CO, H_2O), the Picarro Inc. G5310 CRDS was chosen and purchased (SN: JKADS5054). According to the manufacturer, the analyser offers the following specifications:

Measurement range: 0 – 1500 nmol mol^{-1} N_2O, 0 – 1500 nmol mol^{-1} CO, 0 – 3% H_2O

Precision: 1–500 nmol mol^{-1} N_2O: <0.2/<0.04/<0.02 nmol mol^{-1} (5 s/5 min/1 hour)
1–400 nmol mol^{-1} CO: <0.2/<0.04/<0.02 nmol mol^{-1} (5 s/5 min/1 hour)
H_2O: 40/6 µmol mol^{-1} (5 s/5 min)

Flow rate: 100 mL min^{-1}

Before field deployment the new analyser was tested at Empa for precision, offset, non-linearity and interference with other gases (CO_2 and H_2O). These tests were carried out in cooperation with the GAW World Calibration Center (WCC) for O_3, CO_2, CH_4 and CO at Empa, which maintains a series of gas standards certified by NOAA ESRL GMD.

The G5310 analyser operates with a frequency of one measurement in 3 seconds. From two independent measurement series, the Allan precision of the Picarro Inc. analyser for measurements of a compressed air cylinder was estimated as: 0.086 nmol mol^{-1}, 0.020 nmol mol^{-1}, 0.008 nmol mol^{-1} for N_2O, and 0.105 nmol mol^{-1}, 0.019 nmol mol^{-1}, 0.008 nmol mol^{-1} for CO and for averaging times of 5 s, 5 min and 1 hour, respectively. These values agree well with the specifications given by Picarro Inc.

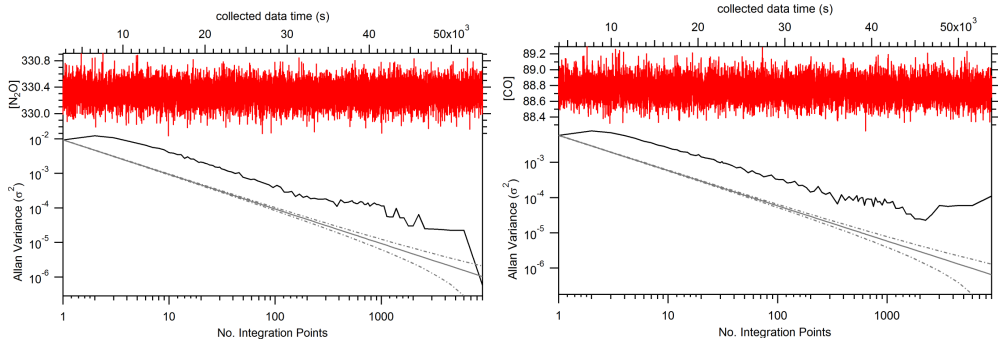

Figure 1: Allan precision of the Picarro Inc. G5310 CRDS measuring compressed air in the laboratory on 2016-12-07: (left) N_2O and (right) CO.

Offset and linearity of the analyser were checked by a series of measurements using four different NOAA ESRL GMD gas standards at WCC-Empa. In order to correct any analyser drift during these measurements, compressed air was measured between two standard gas measurements. The required drift corrections were small (<0.1 nmol mol^{-1} d^{-1} N_2O). The response of the analyser proved to be very linear with absolute residuals to a linear response smaller than 0.075 nmol mol^{-1}and 0.05 nmol mol^{-1} for N_2O and CO over a range of 323 to 357 nmol mol^{-1} N_2O and 110 to 484 nmol mol^{-1} CO, respectively (Figure 2).

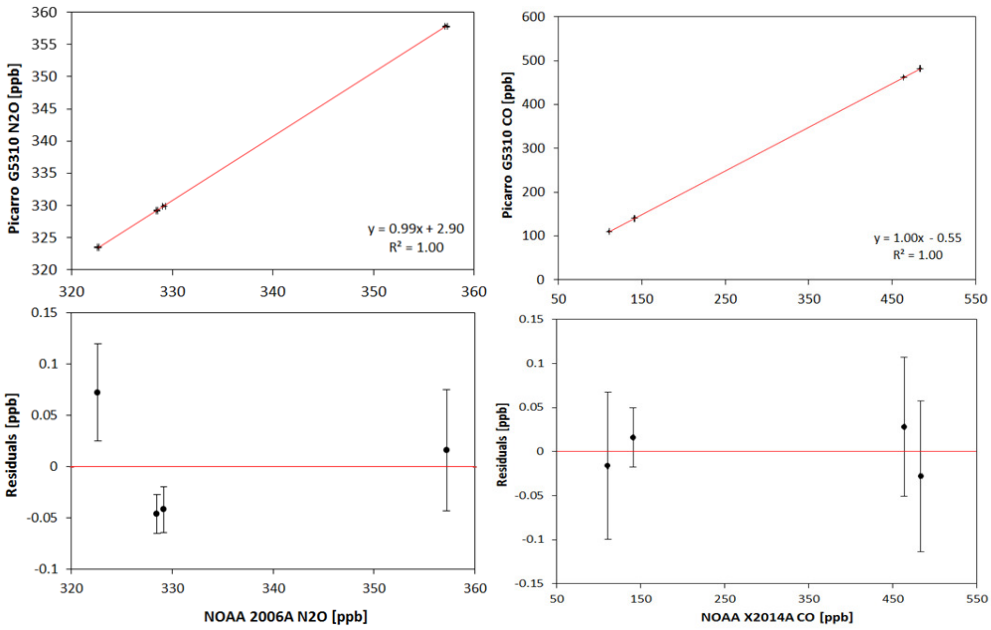

Figure 2: Linearity tests of the G5310 analyser using different NOAA ESRL GMD certified standard gases: (left) for N_2O (right) for CO. Error bars indicate the standard deviation of 3 s raw data.

To quantify the potential interference of CO_2 and H_2O with the measurements of N_2O and CO two sets of experiments were carried out; in short the same compressed air standard was analysed while CO_2 and H_2O concentrations were varied. To achieve different levels of CO_2, pure CO_2 was added in a controlled way through a mass flow controller to the sample gas stream. The resulting dilution of the N_2O in the sample gas was corrected for. A very small influence of CO_2 on the N_2O measurements in the order of 0.08 nmol mol^{-1} N_2O for a CO_2 increase of 300 µmol mol^{-1} and in the range < 1000 nmol mol^{-1} CO_2 could not be ruled out (Figure 3), whereas no systematic interference of CO_2 was observed with the CO measurements.

For H_2O the G5310 analyser performs a built-in correction of the N_2O and CO measurements (parameters N2O_dry, CO_dry). This internal correction efficiently removes the interference with H_2O and only a negligible remaining interference of 0.06 nmol mol^{-1} N_2O and 0.13 nmol mol^{-1} CO per percent H_2O was observed (Figure 4). Hence, no further H_2O interference correction was applied.

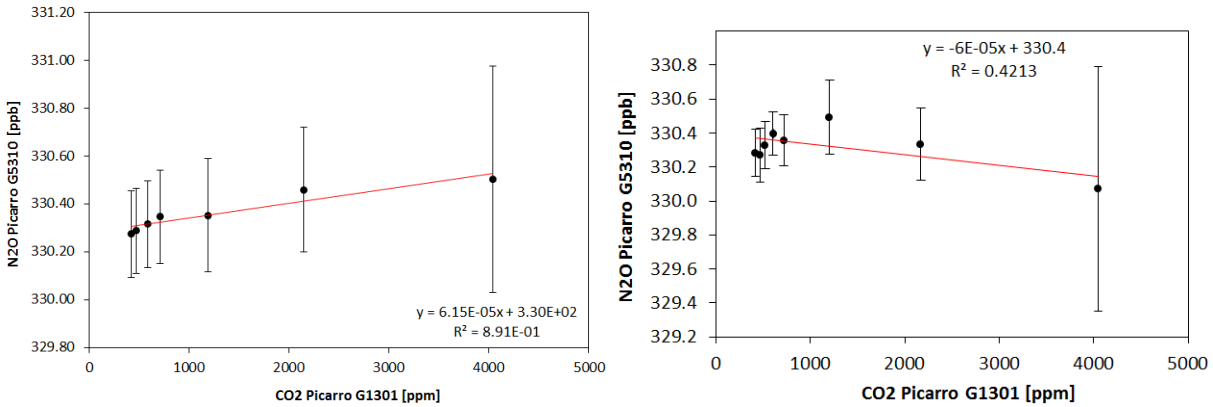

Figure 3: Interference of CO_2 with N_2O measurements by G5310: (left) on 2016-11-03 with drift correction, (right) on 2016-12-07 with drift correction. Error bars indicate the standard deviation of 3 s raw data.

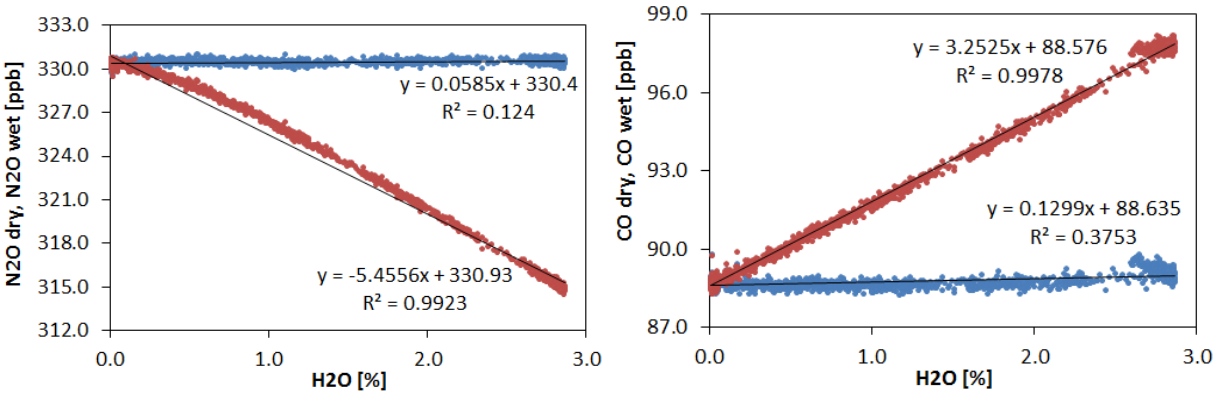

Figure 4: Interference of H_2O with (left) N_2O and (right) CO measurements by G5310. Red dots denote the uncorrected raw measurements, blue dots the values after analyser-internal correction.

2.1.2 Field deployment

For the continuous operation and automated calibration of the G5310 analyser in the field, it was necessary to build a sample gas switch unit (Figure 5), which allows the analyser to switch between different calibration and target gases, on the one hand, and ambient air samples from different inlet lines of the Beromünster tall tower on the other hand. The switch unit was tested for 12 days in the laboratory before field deployment.

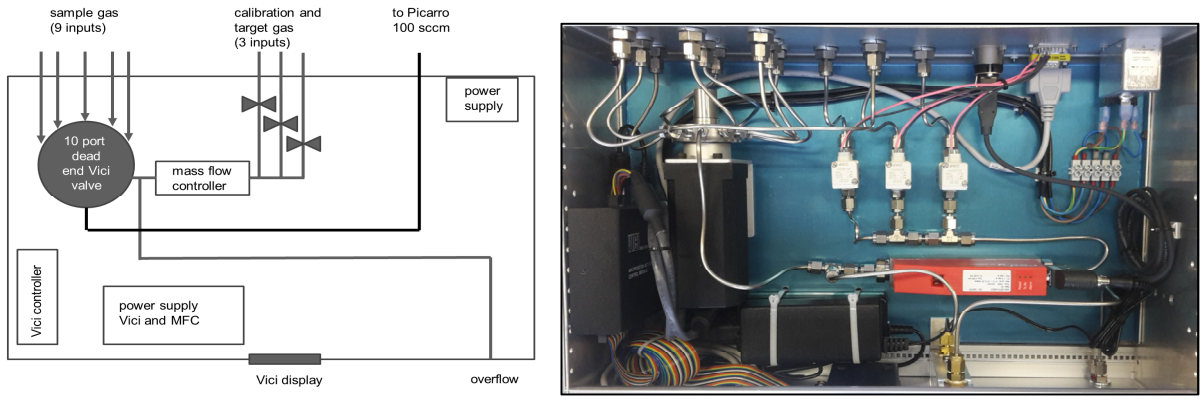

Figure 5: Schematic and picture of sample gas switch unit used for in-field operation of the G5310 analyser.

For the ambient air sampling at the Beromünster tower new inlet flush pumps had to be installed to avoid disturbances of the existing GHG measurements (CO_2, CH_4, CO) by the University of Bern. The main components of the re-configured inlet systems are shown in Figure 6. Identical configurations were installed for all five existing inlet lines. In addition, sampling from the NABEL inlet on the housing top (5 m above ground) was possible, but without the need for additional installations.

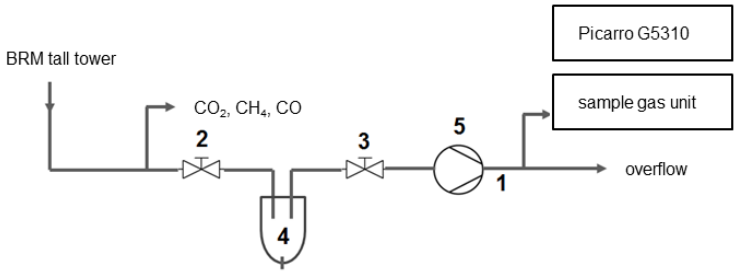

Figure 6: Schematic of gas flow for inlet lines mounted on Beromünster tall tower. 1) decarbon tubing, 2) on/off valve, 3) control valve, 4) liquid water trap, 5) membrane pump (KNF Neuberger AG, Type N 838 ANE).

Compressed air calibration gases were prepared and stored in aluminium cylinders (50L, Matar S.r.l., Mazzano, Italy) with brazen pressure reduction valves. Different filling strategies were used to achieve a useful range of N_2O levels embracing the expected range of concentrations in the field. Two cylinders were filled with ambient air to a pressure of ~140 bar at the NABEL site Rigi-Seebodenalp using a

modified, oil-free compressor (1S3B-6EH-AQS, RIX Industries, Benicia, CA, USA). Before compression, the air was dried using two magnesium-perchlorate cartridges (340 g each). One of the cylinders was enriched before filling with 250 mbar of a known standard gas (25 ppm N_2O, 200 ppm CH_4, 50 ppm CO in 20.95% O_2/ 0.93% Ar rest N_2, Messer Schweiz AG). Another cylinder was filled with commercially available compressed air (Messer Schweiz AG). Gas cylinders filled in this way were calibrated at Empa-WCC against NOAA standards and referenced on the WMO-N2O-X2006A scale.

A two point calibration strategy was implemented for the in-field observations. Two calibration standards (low/high) were measured every 25 hours, each for 16 minutes. In addition, a target gas was measured every 6 hours for 16 minutes to monitor the data quality.

2.1.3 In-field performance

In general the analyser performed reliably and without much requirement for maintenance and interventions. The only regular maintenance was the refilling of the water tank, which is part of the cooling cycle for the MIR QC laser. The acquired data were transferred automatically back to Empa and were analysed in near-real-time, allowing for a quick response in case of instrument malfunction.

Only one major measurement interruption occurred during the first year of operation between 2017-09-12 and 2017-11-06 due to the failure of the internal water pump for the laser cooling. The analyser was taken back and repaired at Empa with the advice received from Picarro Inc. The length of the interruption is explained by delays in receiving the required spare parts from the US.

Furthermore, some calibration issues arose due to leaks in the connectors (decarbon tubing) between the calibration gases and the valve switch unit. Two times one of the two calibration gases completely ran out before the leaks were detected. The first time, the empty gas cylinder was replaced quickly with a spare cylinder (2017-11-15) and the two-point calibrations could be carried out as usual. The second time, no suitable spare cylinder was available and a new calibration standard had to be prepared first. Hence, between 2018-01-16 and 2018-03-24 the calibration was only carried out as a one point span calibration. The influence on the measurement uncertainty is discussed below.

The overall in-field performance of the analyser is summarised in Figure 7. Different measures of uncertainty are provided. These are, on the one hand, propagated from the uncertainties of the calibration gases and the calibration procedure (random, non-random, and combined uncertainty) and, on the other hand, estimated from the calibrated target gas observations (difference, and 10 day RMSE). Except for the period when only one calibration gas was operated, the different uncertainty measures (combined uncertainty vs. target difference) agreed fairly well, i.e. the target differences mostly fell within the band given by the combined uncertainty. When using the 10-day RMSE of the target differences as our best estimate of measurement uncertainty, this was always smaller than 0.1 nmol mol^{-1} and on average about 0.05 nmol mol^{-1} for the N_2O observations. Large values of up to 0.09 nmol mol^{-1} were only reached during a short period in November 2018. For CO similar target accuracies of smaller than 0.1 nmol mol^{-1} were achieved. These values were only exceeded during the period when the analyser was operated with a single calibration gas and only a scale calibration was carried out.

In conclusion, the analyser demonstrated an outstanding performance and fulfilled the very stringent uncertainty requirements of the WMO GAW of 0.1 nmol mol^{-1} N_2O and 2 nmol mol^{-1} CO and for using the observed N_2O mole fractions in an atmospheric inversion.

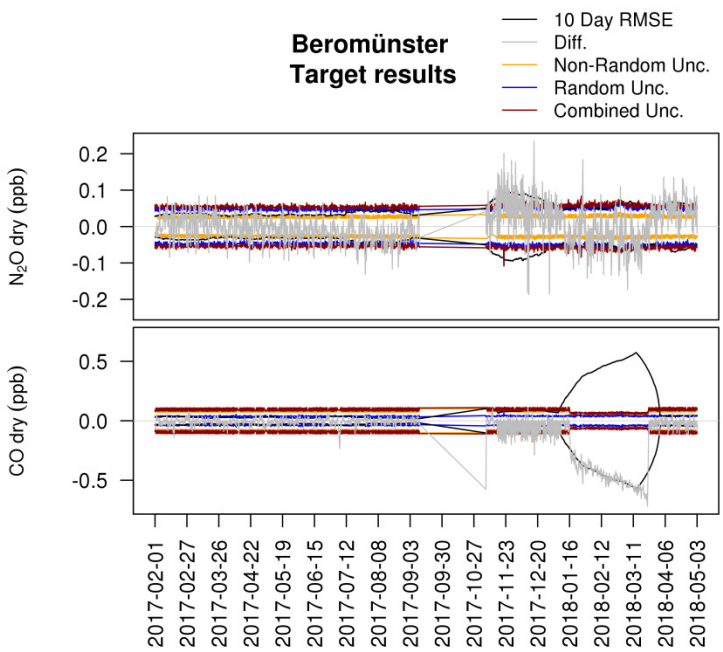

Figure 7: Time series of uncertainty estimates for Beromünster Picarro Inc. G5310 observations (top) N_2O, (bottom) CO. The gray line represents differences between the nominal target gas mole fractions and the calibrated target gas reading of the analyser for individual target measurements, whereas the black line gives a 10-day running RMSE of these quantities. The yellow and blue line give estimates of the non-random and random uncertainty of the analyser propagated from the uncertainties of the calibration gases and the calibration procedure, and the red line represent the combined uncertainty resulting from the random and non-random contributions.

2.1.4 Data processing and baseline estimation

The G5310 N_2O and CO raw data were recorded with a frequency of approximately 1/3 Hz. From the raw data 1-minute aggregates were created and categorized into different measurement types (ambient, calibration gases). After each switch of the sampling line between different inlet heights and calibration gases, five minutes of recorded data were discarded to allow the analyser cell to be sufficiently flushed by the new sample or calibration gas. Calibration gas measurements were then further aggregated to an average value per calibration gas measurement. From each pair of complete two-point calibrations a set of offset and span parameters were calculated. For each 1-min ambient air and target gas sample offset and span values were interpolated from the two closest calibration points and applied to the raw data to obtain calibrated 1-min data and uncertainty estimates.

Calibrated ambient 1-min data were further aggregated to 1-hour averages separated by inlet height. From the 1-hour averages baseline fits to the data were estimated using the method of Robust Estimation of Baseline Signal (REBS, Ruckstuhl et al., 2012). Next to a smooth curve fit to the observations, which represents baseline levels, the method provides an uncertainty estimate of the baseline. Finally, 1-hour data and baseline estimates were further aggregated to 3-hourly averages for the use in the inverse modelling (the temporal resolution of model simulations). Since atmospheric transport models are known to best reproduce afternoon mole fractions at sites in relatively flat terrain, only the Beromünster N_2O observations between 12:00 UTC and 18:00 UTC were used in the inversion.

2.2 Additional nitrous oxide measurements in Switzerland and southern Germany

Next to N_2O observations from Beromünster those of the high-altitude site Jungfraujoch in the Swiss Alps and those of the Schauinsland observatory in the Black Forest were available for this study.

At Jungfraujoch N_2O is measured continuously with an off-axis integrated cavity output spectrometer from Los Gatos Research Inc. (N_2O/CO-23r). The inlet is located at 3580 m asl, approximately 5 m above the roof of the Sphinx laboratory. Data are recorded as 5-second averages. A working gas is measured every 3 hours to account for short-term sensitivity changes of the analyser. Three reference gases are measured every 3 days for calibration. Two target tanks are analysed every one and two days,

respectively, for additional quality control. Each reference gas is measured for 25 minutes. These analyses reveal a mean standard deviation of 1-minute averages (random uncertainty) usually smaller than 0.04 nmol mol^{-1}. Target gas accuracy was usually smaller 0.1 nmol mol^{-1}. At the UBA station Schauinsland an OA-ICOS analyser developed by Los Gatos Research is running since January 2015 in parallel with a GC system. Here, only the data from the Los Gatos analyser were used, which were assigned an average measurement uncertainty of 0.1 nmol mol^{-1}. Data from both sites are reported on the WMO-N2O-X2006A scale.

Data from both sites were processed in the same way as data from Beromünster to estimate baseline levels and their uncertainties and to provide 3-hourly aggregates for the inverse modelling. In contrast to Beromünster, the Jungfraujoch and Schauinsland sites are mountain-top sites, which are often influenced by topography-related, thermally induced flow phenomena during the day. These local flow features are often not well reproduced by atmospheric models with grid resolutions as used here. Therefore, for the inversion only nighttime observations between 00:00 UTC and 06:00 UTC were used from these two sites.

2.3 Spatially resolved emission inventory and preparation of a priori emissions

As part of the project the compilation of a spatially resolved N_2O emission inventory for Switzerland was ordered from Meteotest (see detailed report Meteotest, 2017). Here only the most important processing steps are repeated.

The Meteotest inventory is based on EMIS/NIR emission totals for the year 2014 and entries to the Pollutant Release and Transfer Register (PRTR, 3 locations for Switzerland). Spatial grids from previous projects (CO_2, NH_3, organic soils) and additional GIS data (population, land use, etc.) were used to disaggregate emission totals onto a grid with horizontal resolution of 500 m by 500 m covering all of Switzerland. The emission sectors explicitly considered in the inventory represent 97 % of total emissions in EMIS/NIR. The remaining 3 % were equally distributed onto the represented emission sectors. In total 26 different grids for emissions from different sectors were generated. Total gridded emissions for the reference year 2014 were 8.985 Gg yr^{-1}.

Only some of the important spatial allocations are described here. Emissions from leaching were located at water bodies and scaled to the intensity of fertiliser use in a 200 m circumference. The distribution of indirect emissions from (semi-)natural ecosystems was based on the study by Bühlmann et al. (2015), who report a total of 2.5 Gg yr^{-1} for the year 2010. Their findings were recalculated for the year 2014 according to updated nitrogen deposition maps, resulting in total indirect N_2O emissions from (semi-)natural ecosystems of 2.4 Gg yr^{-1}. In contrast the total indirect emissions (including nitrogen input from volatilisation from agricultural soils, manure handling and other sources) in the NIR (FOEN, 2016) amounted to 3.0 Gg yr^{-1}. The difference between these two estimates was assigned to the sector "indirect emissions from agricultural land", which, combined with emissions from leaching, then amounted to 1.15 Gg yr^{-1}. The spatial distribution of the total of all sectors and of three key emission sectors is depicted in its original resolution in Figure 8. In the total emissions one can clearly identify large areas with elevated emissions on the Swiss Plateau and pre-Alpine regions and Alpine valleys as being dominated by direct emissions from agricultural soils. Other emission hot spots can be seen in regions with deep organic soils (Seeland region and upper Rhine valley) and in urban centers (Zurich, Basel, Geneva, Bern). The latter are a consequence of combined emissions from traffic, residential heating and industrial processes. Indirect emissions from (semi-)natural ecosystems are more uniformly spread over the northern parts of Switzerland, but reveal a maximum in Ticino, which is partly related to elevated nitrogen inputs from the Po valley.

Not included in the Meteotest inventory were potential natural emissions of N_2O. Natural emissions are those originating from a mostly undisturbed ecosystem without anthropogenic influences (no deposition of anthropogenic nitrogen). For Switzerland, these emissions are estimated but not reported as part of EMIS (1.37 Gg yr^{-1}), but contain a very high level of uncertainty (Bühlmann, 2014). These estimates may well overestimate the real natural emissions since applied emission factors are taken from outdated studies that were often carried out in regions with anthropogenic nitrogen deposition. The latter complicates the separation of natural from indirect emissions.

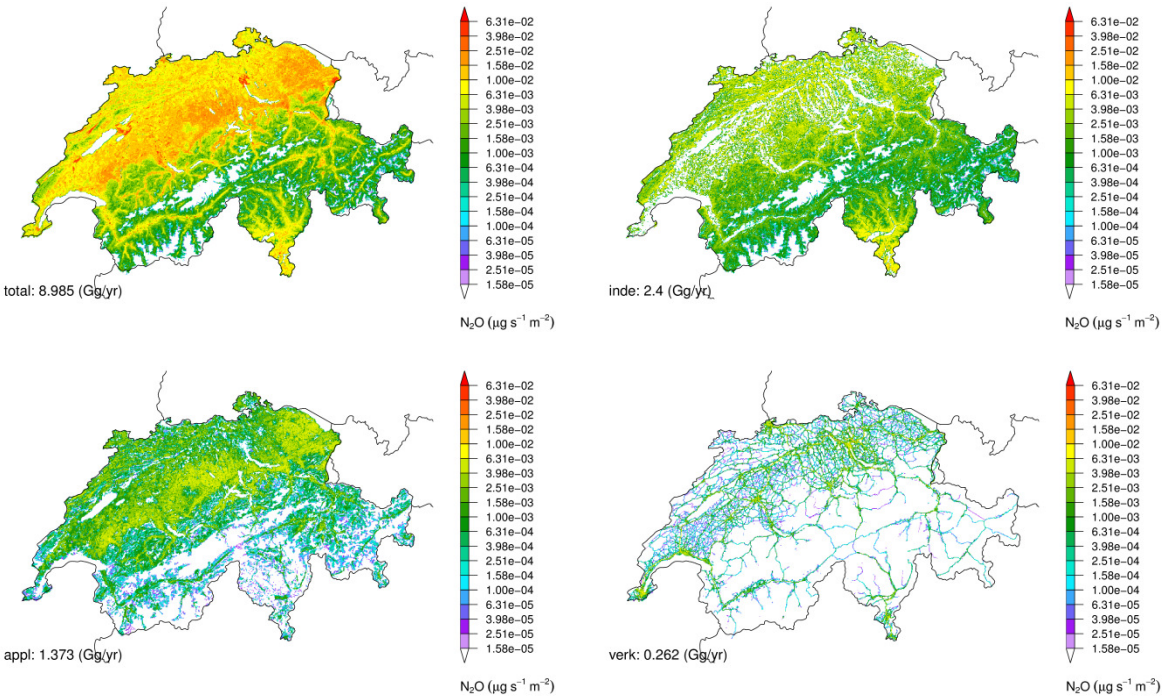

Figure 8: Spatial distribution of Swiss N_2O emissions according to Meteotest inventory: (top left) total emissions, (top right) indirect emissions from (semi-)natural ecosystems, (bottom left) direct emissions from agricultural soils due to application of manure, (bottom right) traffic emissions.

For the inverse modelling a priori emissions outside the Swiss domain are required as well. Therefore, the spatially resolved Swiss N_2O emissions were merged with those from the EDGAR emission inventory (version 4.2_FT2010, Olivier and Janssens-Maenhout, 2012), reference year 2010, to cover areas outside Switzerland. A re-gridding onto the regular longitude/latitude grid, as used by the output of the transport model (see section 2.4), was required in this step as well. Since the inverse modelling in this project was intended to optimise emissions from different sectors, it was also necessary to provide spatially resolved a priori information for different sectors. The EDGAR inventory is available for 11 different emission sectors, which are not identical to the sectors available in the Meteotest inventory. In order to obtain a more uniform categorisation, Meteotest and EDGAR sectors were merged according to Table 1, resulting in 12 merged emission sectors that are comparable between Switzerland and the surrounding countries. One rationale for merging different sectors was their similarity in terms of spatial distribution. Sectors with a similar or identical distribution (if the same gridded information was used to distribute national total emissions in the Meteotest approach) were merged as much as possible, since the sectorial inversion approach cannot be expected to separate such categories.

Table 1: Emission sectors as available in Swiss Meteotest/NIR N_2O inventory and global EDGAR inventory. Merged sectors as used in sectorial inversion.

Merged sectors (abbreviation)	Meteotest description	NIR sector	NIR emisions (Gg yr^{-1})	EDGAR description	EDGAR sector
orgs	Organic soils	3 D a 6	0.217	Not available	-
	cement production	1 A 2 f			IPCC_1A1_1A2
	industrial combustion	1 A 2 g viii			IPCC_1A1_1A2
industrialHeating	furnaces, waste incinerator, other industrial	1 A 1 a	0.130	Power plants/ind. combustion	IPCC_1A1_1A2
	agricultural machinery	1 A 4 c ii			IPCC_1A3a_c_d_e
	construction machinery	1 A 2 g vii		non-road transport	IPCC_1A3a_c_d_e
transport	road traffic	1 A 3	0.302	road transport	IPCC_1A2b
	heating, agriculture	1 A 4 c i			IPCC_1A4
	heating, commercial	1 A 4 a i			IPCC_1A4
heating	heating, private	1 A 4 b i	0.168	heating of buildings	IPCC_1A4
refinery	refineries	1 A 1 b; 1 B 2 c 2 1	0.004	refineries	IPCC_1B2a
	nitric acid production	2 B 2			IPCC_2_3
industryAndUse	use in households and hospitals	2 G 3 a; 2 G 3 b	0.160	ind. production and use	IPCC_2_3
manure	manure management	3 B 1 - 3 B 4	0.285	manure management	IPCC_4B
	crop residues/soil organic matter	3 D a 4; 3 D a 5			IPCC_4C_4D
	animal waste on pastures	3 D a 3			IPCC_4C_4D
	synthetic fertiliser use	3 D a 1 a; 3 D a 1 b; 3 D a 2 c; 3 D a 7			IPCC_4C_4D
directAgri	manure application	3 D a 2 a	3.481	direct agri. soil emissions	IPCC_4C_4D
	leaching	3 D b 2			IPCC_4D3
indirectAgri	other indirect emissions from agri. soils	CRF-Table 6	1.143	indirect agri. emissions	IPCC_4D3
wasteBurning	illegal waste burning	5 C 1 a; 5 C 2 i; 5 C 2 ii	0.007	field burning of agri. residues	IPCC_4F
	industrial fermentation	5 B 1			IPCC_6
	wastewater treatment (2 point sources)	5 D 1			IPCC_6
	sewage sludge burning	5 C 1 b iv			IPCC_6
waste	wastewater treatment (communal)	5 D 1	0.591	waste	IPCC_6
indirectNat	indirect emissions from (semi-)natural ecosystems	3 B 5 a; 3 D b 1	2.369	indirect from non-agri. soils	IPCC_7B_7C

The spatial distribution of the six emission sectors with the largest contribution to the total Swiss N_2O emissions are shown in Figure 9. Here, these emissions were aggregated/interpolated onto the output grid of the FLEXPART transport model (0.02° by 0.015° horizontal resolution). The dominance of emissions from agricultural soils, whether from direct or indirect nitrogen deposition, becomes very apparent in Switzerland but also in the surrounding countries. The invaluable added information of the Meteotest inventory as compared with the EDGAR inventory is striking for all emission sectors and most pronounced for indirect emissions from (semi-)natural ecosystems. For this sector EDGAR only provides one uniform flux per country, whereas the Meteotest inventory clearly reflects different land cover types and spatially variable nitrogen deposition loads such as northern vs. southern Switzerland. On the one hand, direct and indirect agricultural soil emissions, but also the direct emissions from manure handling, show very similar spatial patterns within Switzerland. On the other hand, emission sectors like (semi-)natural ecosystems, waste and transport show a distinctly different distribution.

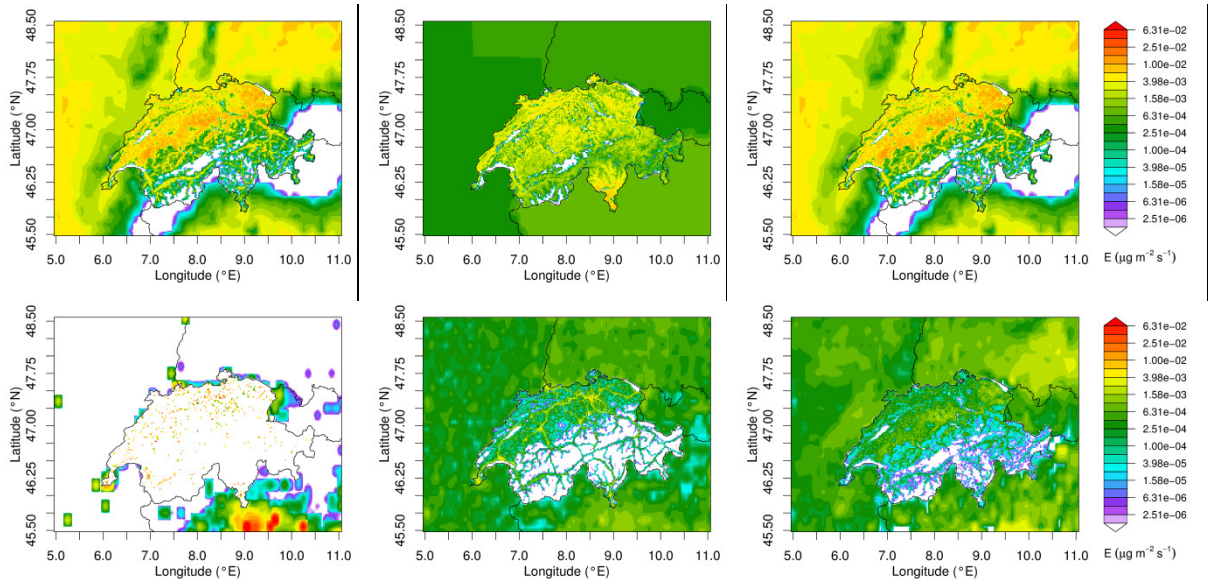

Figure 9: Spatial distribution of N_2O emission inventory (Meteotest/NIR for Switzerland, EDGAR elsewhere) aggregate/interpolated onto FLEXPART output grid for six most contributing sectors: (top left) direct agricultural soils, (top center) indirect (semi-)natural ecosystems, (top right) indirect agricultural soils, (bottom left) waste, (bottom center) transport, (bottom right) manure management.

In order to further analyse the potential of a sectorial inversion approach, the degree of spatial difference between different emissions sectors was evaluated by quantifying the spatial correlation between the sectors. This was done only for the Swiss domain and separately for the sub-regions indicated in Figure 10. These region definitions are later used as sub-regions for the sectorial inversion (see section 2.5.1).

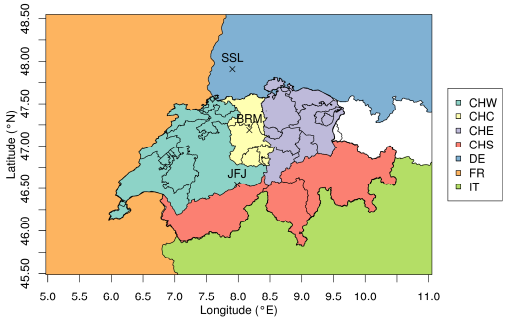

Figure 10: Definition of inversion sub-regions used for SI_BASE inversion. Cantons contained in the Swiss sub-regions are as follows. CHW: Basel-Landschaft, Basel-Stadt, Bern, Fribourg, Genève, Vaud, Jura, Neuchâtel, Solothurn; CHC: Aargau, Luzern, Obwalden, Nidwalden; CHE: Appenzell Ausserrhoden, Appenzell Innerrhoden, Glarus, Zürich, Schaffhausen, Schwyz, St. Gallen, Thurgau, Uri, Zug; CHS: Valais, Ticino, Grisons.

As already suspected from the spatial distribution plots of different emission sectors, the strongest positive spatial correlation exists between all sectors related to agriculture: indirect and direct emissions from agricultural soils and emissions from manure handling. There also exists a considerable positive correlation between these sectors and the illegal waste burning sector. However, the latter contributes less than 1 % to the total Swiss emissions. Furthermore, positive, but weaker, correlations are also seen for direct non-agricultural emissions (transport, heating, industrial production and product use), whereas other sectors like wastewater treatment, industrial heating, refineries, organic soils and indirect (semi-)natural ecosystems show very little positive correlations with any other sector. This correlation pattern is very similar for the other Swiss sub-regions.

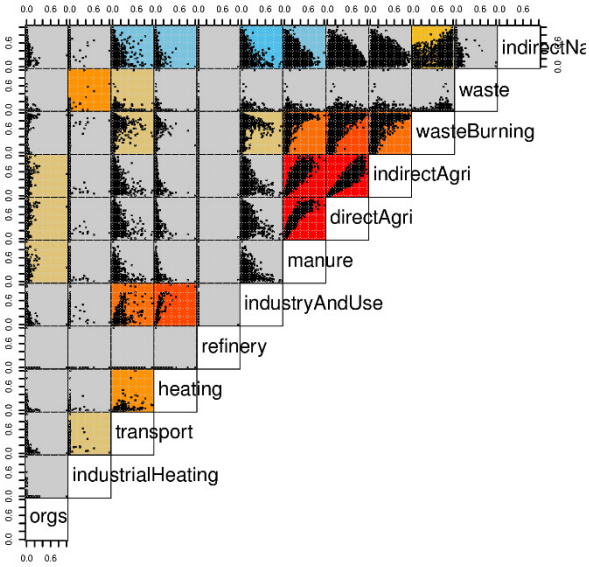

Figure 11: Pairs correlation plot for all emission grid cells in the central Swiss region (CHE). Red (blue) colours indicate a positive (negative) correlation; the darker the colour the stronger the correlation.

2.4 Atmospheric transport simulations

The transport of N_2O from the location of emission to the measurement sites was simulated using the Lagrangian Particle Dispersion (LPDM) model FLEXPART-COSMO (Henne et al., 2016; Oney et al., 2015). This version of the FLEXPART model system was adapted for the use of meteorological input data generated by the numerical weather prediction model (NWP) COSMO. Here, the hourly available COSMO analysis fields operationally generated by MeteoSwiss were used to drive the FLEXPART-COSMO simulations. More specifically, the COSMO output with a horizontal resolution of approximately 7 km x 7 km (COSMO7) was used. The COSMO7 grid covers large parts of Western and Central Europe, which is a sufficiently large domain to simulate the incremental increase of N_2O affecting an air mass before arriving at the measurement sites.

FLEXPART-COSMO simulations were carried out in a time-inverted backward mode, meaning that model particles were released at the location of the measurement sites (receptors) and then their transport in the atmosphere was followed backward in time. The transport description in FLEXPART-COSMO includes advection by the mean flow, stochastically described turbulent mixing and vertical mixing in sub-grid scale cumulus convection. First order decay processes of the transported substance can be considered as well but were not applied here due to the exclusive loss of N_2O in the stratosphere. The model calculates residence times of model particles close to the surface, where the simulated air mass interacts with surface emissions (source). Residence times are then transformed into source sensitivities (or source receptor relationships), $m_{i,j}$, which can be directly used to convert a mass emission at the source location, $E_{i,j}$, to an increase in atmospheric mole fractions at the receptor, χ_t. However, this increase in mole fraction does not correspond to the total observed mole fraction, but only provides the contribution of emissions encountered during the period of the transport simulation. Therefore, a baseline or background mole fraction, χ_b, that represents the atmospheric mole fraction at

the terminal location of each model particle in the backward simulation, χ_p, needs to be added. The total simulated mole fraction can then be described as

$$\chi = \underbrace{\sum_{i,j} m_{i,j}\, E_{i,j}}_{\chi_t} + \underbrace{\frac{1}{P}\sum_{p} \chi_p}_{\chi_b}, \quad (1)$$

where *i,j* are the grid indices of the horizontal model output grid, and *P* is the total number of model particles in the simulation.

The mole fractions at the terminal particle location could be taken from a three-dimensional field of mole fractions available at a larger scale (either large-scale model output or observation-based products). If such fields are not available, as was the case here, the baseline mole fraction as a whole, χ_b, can also be taken from other observational data, for example from another measurement site that is often sampling baseline conditions or from a statistically filtered time series, which excludes most recent emission influences (see baseline estimation in section 2.1.4).

For the current study, source sensitivities were calculated at 3-hourly intervals for all measurement locations. For each interval and release location 50'000 model particles were released and followed four days backward in time or until they left the COSMO7 domain. The COSMO7 horizontal resolution is not sufficient to give a realistic picture of the complex topography in Switzerland. Therefore, the actual elevation of a measurement site often does not agree with the model topography. This is especially true for measurement sites that are situated at elevated locations, as is the case for all sites used in this study. The question arises of where to release model particles. Either this could be done at the same height above ground as the sampling is done in reality or at the exact elevation above sea level. For elevated sites, the former usually results in an unrealistically low mean height of model particles and consequently an overestimation of source-sensitivities, whereas the latter in general seems to be the more correct approach. It may, however, underestimate the influence of topography on the flow. A feasible compromise is to release model particles in the middle between the model topography and the actual elevation. Here, this approach was followed for all measurement sites (see Table 2). In addition, secondary release heights representing the true elevation of the site were used for the sites Beromünster and Schauinsland. The uncertainty of the transport simulations resulting from this topographic mismatch are considered in the inverse modelling by always running two sets of inversion, one (referred to as low) using the lower release heights for Beromünster and Schauinsland and the other (high) using the upper release heights.

Source sensitivities were generated by FLEXPART-COSMO on two different horizontal grids, one covering the complete COSMO7 domain with a horizontal resolution of 0.16° x 0.12°, the other covering the larger Alpine area with a horizontal resolution of 0.02° x 0.015°. Output was stored for every 3-hourly time slice along the four-day backward simulations. For both grids a sampling height of 50 m was chosen, which agrees with the minimum mixing height in the model. The sampling height gives the elevation above model ground for which the source sensitivities are calculated. Only model particles residing between the model ground and the sampling height are evaluated for source sensitivities. This assumes that all emissions enter the atmosphere at this height level, which is a reasonable assumption for N_2O emissions.

Table 2: Overview of measurement locations, sampling heights and FLEXPART-COSMO release heights.

Station	ID	Longitude (°E)	Latitude (°N)	Elevation (m a.s.l.)	Inlet height (m a.g.l.)	COSMO7 elevation (m a.s.l.)	FLEXPART release height (m)
Beromünster	BEO	8.1755	47.1896	798	2, 5, **212**	615	212 a.g.l. 1010 a.s.l.
Jungfraujoch	JFJ	7.9851	46.5475	3580	5	2650	3100 a.s.l.
Schauinsland	SSL	7.9167	47.9000	1205	10	750	980 a.s.l. 1205 a.s.l.

2.5 Inversion frameworks

Two different inverse modelling frameworks were set up for estimating Swiss N_2O emissions. Both rely on the simulated source sensitivities and atmospheric observations, but they differ in terms of the structure of emissions that are optimised. The aim of both frameworks is to optimise the emissions with a sufficiently fine temporal resolution in order to capture the expected temporal variability. As explained above, variability may occur at small time scales due to fast changes in environmental controls (temperatures, precipitation) and due to management interventions. The atmospheric inversion cannot be expected to capture this variability on a daily basis, but variability on a monthly to seasonal scale should be captured to avoid biases.

The first inverse modelling framework is the one previously applied to Swiss CH_4 emissions (Henne et al., 2016). It optimises the emissions on an irregular spatial grid (grid inversion). Grid cell sizes are determined proportionally to total annual source sensitivities, with smaller grid sizes in areas with large source sensitivities and vice versa. The number of grid cells to optimise in this setup can be varied, but in order to separate Swiss emissions properly from those of the neighbouring countries, several hundred grid cells are required (620 in the GI_BASE inversion, see below). In order to cover temporal variability in the emissions, the number of grid cells needs to be multiplied with the number of times for which the emissions should be optimised. If monthly optimisation is desired this would result in a total number of 8680 unknowns for the 14 month period investigated here. Compared with the number of available atmospheric observations for the same period (2279 3-hourly averages for the selected time of day and the three sites) the number of unknowns is very large and the problem would be largely under-determined. Therefore, N_2O emissions were only optimised on a seasonal scale when using the gridded inversion approach.

The second inversion framework was newly implemented for this study and is described in detail in section 2.5.1. In contrast to the first approach, it does not optimise the emissions on a spatial grid but optimises scaling factors for different sub-regions (8 in the SI_BASE setup) and different emissions sectors (12 in the SI_BASE setup). Hence, only 96 unknown emission scaling factors have to be optimised at a time. Multiplied by the number of months in the investigated period, 1344 emission scaling factors would need to be optimised. This is a much more reasonable number of unknowns than in the case of the grid inversion. Hence, monthly varying emissions were optimised by the sector inversion.

Both inversion frameworks use Bayesian inference to optimise a state vector, x, which contains unknowns relating to the emissions and to baseline mole fractions. The model-derived source sensitivities are compiled in the matrix $\mathbf{M}$, which multiplied with the state vector, x, provides the simulated mole fractions at the receptor locations. The Bayesian approach then defines the following cost function

$$J = \frac{1}{2}(x - x_b)^T \mathbf{B}^{-1}(x - x_b) + \frac{1}{2}(\mathbf{M}x - \chi_o)^T \mathbf{R}^{-1}(\mathbf{M}x - \chi_o), \quad (2)$$

where x_b represents the a priori state of the state vector, χ_o are the atmospheric observations, and $\mathbf{B}$ and $\mathbf{R}$ are covariance matrices that describe the uncertainty of the a priori and the data-mismatch uncertainty, respectively. Minimising the cost function by varying the state vector x yields the desired a posteriori state. The analytical solution to the minimisation problem is given by

$$x = x_b + \mathbf{B}\mathbf{M}^{\mathbf{T}}(\mathbf{M}\mathbf{B}\mathbf{M}^{\mathbf{T}} + \mathbf{R})^{-1}(\chi_o - \mathbf{M}x_b). \quad (3)$$

The uncertainty of the a posteriori state is given by the covariance matrix $\mathbf{A}$,

$$\mathbf{A} = \mathbf{B} - \mathbf{B}\mathbf{M}^{\mathbf{T}}\mathbf{S}^{-1}\mathbf{M}\mathbf{B}, \quad (4)$$

where $\mathbf{S} = \mathbf{M}\mathbf{B}\mathbf{M}^{\mathbf{T}} + \mathbf{R}$. Any aggregation of elements of the state vector, x, for example to derive national total emissions, will need to take the a posteriori covariance, $\mathbf{A}$, into account to derive the uncertainty estimate for the aggregated quantity.

Furthermore, a simple, but not necessarily sufficient, test of the setup of the covariance matrices can be formulated. Due to the Gaussian assumptions applied in the solution of equation (2) it can be shown that at its minimum J should follow a χ^2-distribution with a mean value of N/2, N being the number of observations in χ_o. Hence, one can define a χ^2-index based on the value of J at the a posteriori state

$$\chi^2_I = \frac{2J(x)}{N}, \quad (5)$$

which, for well-defined covariance matrices, should be close to 1 (Berchet et al., 2013).

In addition, also a measure for the number of independent pieces of information gained through the inversion can be evaluated. The matrix

$$\mathbf{C} = \mathbf{B}\mathbf{M}^{\mathbf{T}}\mathbf{S}\mathbf{M}, \tag{6}$$

is known as the averaging kernel of the inverse retrieval The trace of **C** gives its degree of freedom (DF), which represents the desired number (Rodgers, 2000).

2.5.1 Sectorial resolved inversion (sector inversion)

For the sectorial inversion, the state vector does not directly contain emission fluxes, but emission scaling factors. Their use is motivated in the following. Starting with equation (1) for the mole fractions simulated by an LPDM for a specific time, we now split the emissions into *K* different emission sectors. The contributions from these sectors can be linearly added, hence, the summation of the first term of equation (1) now runs over space, *i,j*, and emission sectors, *k*. Furthermore, a scaling factor f_k, is introduced, which is a constant in space for each sector and allows for the optimisation of a reduced set of unknowns in the inversion, is introduced

$$\chi = \underbrace{\sum_{i,j,k} m_{i,j}\, f_k E_{i,j,k}}_{\chi_t} + \underbrace{\frac{1}{P}\sum_{p} \chi_p}_{\chi_b}. \tag{7}$$

The order of summation of the first term can be exchanged. Summing each sector first over space yields the mole fraction contribution of this sector at the location of the receptor, χ_k,

$$\chi = \sum_{k} f_k \underbrace{\sum_{i,j} m_{i,j}\, E_{i,j,k}}_{\chi_k} + \chi_b. \tag{8}$$

Hence, the equation can now be re-written as the sum of the mole fractions by sector multiplied by the scaling factors plus the baseline contribution

$$\chi = \sum_{k} f_k \chi_k + \chi_b. \tag{9}$$

For a time series of simulated mole fractions, equation (9) can be written in matrix notation

$$\begin{pmatrix} \chi_1 \\ \vdots \\ \chi_T \end{pmatrix} = \begin{pmatrix} \chi_{1,1} & \cdots & \chi_{1,K} & \varphi_{1,1} & \cdots & \varphi_{1,L} \\ \vdots & \ddots & \vdots & \vdots & \ddots & \vdots \\ \chi_{T,1} & \cdots & \chi_{T,K} & \varphi_{T,1} & \cdots & \varphi_{T,L} \end{pmatrix} \begin{pmatrix} f_1 \\ \vdots \\ f_K \\ \chi_{b,1} \\ \vdots \\ \chi_{b,L} \end{pmatrix} = \mathbf{M}x, \tag{10}$$

where *T* is the number of simulations (time and space), $\chi_{b,l}$ are baseline mole fractions at different times, *l*, and $\varphi_{t,l}$ are factors folding these baseline mole fractions into the simulated total mole fractions, χ_t. The $\varphi_{t,l}$ describe a linear interpolation between two baseline values in time (Stohl et al., 2009).

The matrix in equation (10) provides the sensitivity matrix, **M**, as required for the Bayesian evaluation of equation (2). The column vector containing the f_k and $\chi_{b,l}$ is the state vector, *x*, that will be optimised by the inversion. Hence, the state vector contains both, elements that describe the emission and baseline influence onto the simulated mole fractions.

For the sector inversion approach, the final a posteriori emissions can then be derived from the a posteriori state of f_k multiplied by $E_{i,j}$ or, if one is not interested in the spatial distribution of E, simply the sum over $E_{i,j}$ multiplied by f_k. If the $E_{i,j}$ represent the a priori state of the emissions the a priori value of all f_k would simply be 1. However, one is not limited to this assumption and can assign other a priori values too.

If emissions are allowed to vary in time, the matrix **M** needs to be extended and additional sets of f_k need to be introduced for different times. If the length of each emission period is large compared to the transport time in the LPDM, it can be assumed that the $\chi_{t,k}$ only depend on one set of f_k at a time. Otherwise, a temporal interpolation between two emission states would need to be considered as well,

which was not done in the current implementation, since the transport time of four days was deemed short enough compared to the envisaged temporal resolution of the emissions of one month.

2.5.2 Parameters describing covariance structures

As for the gridded inversion the sectorial inversion requires a realistic setup of the covariance matrices **R** and **B**. Similar concepts for their design as for the gridded inversion (Henne et al., 2017) were followed here. In the SI_BASE inversion the data-mismatch uncertainty was estimated iteratively from the model residuals at each site, assuming that the diagonal elements of the covariance matrix can be described as the quadratic sum of the observation uncertainty, σ_o, a minimum model uncertainty, σ_{min}, and an additional model uncertainty, σ_{srr}^2, that is variable over time and is proportional to the a priori simulated mole fractions, $\chi_{b,i}$,

$$R_{i,i} = \sigma_{o,i}^2 + \sigma_{min}^2. + \sigma_{srr}^2 \chi_{b,i}^2. \quad (11)$$

In addition, an exponential decay of the covariance between two different times using a temporal correlation length scale, τ_o, was manually set to a value of 0.25 days. This value was evaluated against the auto-correlation function of the model residuals of the a priori simulation, showing a reasonable prediction of the auto-correlation by the exponential decay.

The diagonal elements of the emission part of the a priori covariance matrix, **B**, were set proportionally to the emissions. Two exponential factors were used to describe the temporal and spatial covariance between emission elements and to set the off-diagonal elements of the covariance matrix. The temporal scale, *T*, and spatial scale, *L*, were used to set the degree of covariance. In the sector inversion, spatial correlation was only considered for emissions from the same sector, but from different subregions. The proportionality factor, temporal and spatial length scales were adjusted in such a way that the total Swiss a priori uncertainty, σ_{Eb}, agreed with the bottom-up uncertainty given in the NIR (19.8 %, 1-σ level).

Similarly, the uncertainty of the a priori baseline was described by a constant, site-specific uncertainty, σ_B, assigned to the remaining diagonal elements of **B** and an exponential decay of the covariance with time, using a time scale τ_b. The a priori baseline, σ_B was taken from the REBS fit to the observational data from Jungfraujoch. The time scale τ_b was set to 30 days in the SI_BASE inversion.

In addition to the described semi-empirical setup of covariance parameters, a more objective approach for their estimation was implemented through the method of maximum likelihood (Henne et al., 2017; Michalak et al., 2005). These cases are reported as part of the sensitivity inversions, discussed in the following section.

2.6 Setup of sensitivity inversions

The analytical description of uncertainties in the Bayesian inversion often does not cover all aspects of uncertainty. Various factors that influence the setup of the inversion framework may introduce additional sources of uncertainty (structural uncertainty) that are not covered by the analytical framework. These structural uncertainties can be uncovered by additional sensitivity inversions that vary certain aspects of the inversion setup.

The sensitivity inversions evaluated in this study are summarised in Table 3. For all sensitivity inversions two versions were performed, one using the source sensitivities derived from the transport simulations with low model particle releases and the other using those from the high particle releases. The base setup for the sector inversion (SI_BASE) uses a sub-division of the Swiss domain into 4 separate regions (Figure 10), monthly emission resolution, and the covariance parameters described in section 2.5.2. Similarly, a base setup was constructed for the gridded inversion (GI_BASE) optimising emissions by season and using the same covariance parameters as for the SI_BASE inversion. In a first set of sensitivity inversions, the regional sub-division within Switzerland was varied from 3 to 6 regions (SI_CH3, SI_CH6). The influence of the temporal resolution of the emissions on the estimate of annual total emissions was investigated through a sector inversion with only seasonal emission resolution (SI_seas). This sensitivity inversion also allows for a more direct comparison with the grid inversion, which was run with seasonal resolution by default. The SI_BASE inversion did not include any a priori information on the temporal variability of the emissions. The influence of this flat time profile was

investigated by a sensitivity inversion for which a seasonal cycle was prescribed in the a priori (SI_VarPrior), using the a priori time profile applied in Thompson et al. (2014) for Europe. In the SI_BASE inversion, the same relative uncertainties were assigned to all emission sectors. This was varied in an additional inversion (SI_SecUnc), in which the uncertainties were set up by sector according to values given in the Swiss NIR. Furthermore, the influence of the chosen uncertainty of the baseline was tested by another set of sensitivity inversions for which σ_B was increased/decreased by a factor of 2. This was done for the sector inversion (SI_uBLlow, SI_uBLhigh) and the grid inversion (GI_uBLlow, GI_uBLhigh).

Finally, the SI_MLopt sensitivity inversion used a set of covariance parameters as obtained from the maximum likelihood method. In addition, SI_MLopt_w/o_BL used the same approach but excluded the baseline-related parameters (σ_B, τ_b) from this optimisation and used the SI_BASE settings for these instead.

Table 3: Settings of sensitivity inversions. Each sensitivity inversion was carried out twice: once with low and once high particle release heights in the transport model.

ID	Type	Temporal resolution of emissions	# Swiss regions	Covariance parameters	Uncert. by sector	Variable a priori	Baseline uncert.
SI_BASE	Sector	Monthly	4	Prescribed	No	No	1 σ_B
GI_BASE	Grid	Seasonal	-	Prescribed	-	No	1 σ_B
SI_CH3	Sector	Monthly	3	Prescribed	No	No	1 σ_B
SI_CH6	Sector	Monthly	6	Prescribed	No	No	1 σ_B
SI_seas	Sector	Seasonal	4	Prescribed	No	No	1 σ_B
SI_VarPrior	Sector	Monthly	4	Prescribed	No	Yes	1 σ_B
SI_SecUnc	Sector	Monthly	4	Prescribed	Yes	No	1 σ_B
SI_uBLlow	Sector	Monthly	4	Prescribed	No	No	0.5 σ_B
SI_uBLhigh	Sector	Monthly	4	Prescribed	No	No	2 σ_B
GI_uBLlow	Grid	Seasonal	-	Prescribed	-	No	0.5 σ_B
GI_uBLhigh	Grid	Seasonal	-	Prescribed	-	No	2 σ_B
SI_MLopt	Sector	Monthly	4	Optimised	No	No	1 σ_B
SI_MLopt_w/o_BL	Sector	Monthly	4	Optimised	No	No	1 σ_B

3 Explorative data analysis for measurements at Beromünster

For the inverse modelling, only the observations at the top of the Beromünster tall tower were used. Here a brief discussion of the observations at all measurement heights is given in order to characterise these observations and put them into context to the observations from the Jungfraujoch and Schauinsland sites.

The complete N_2O observational data set from Beromünster (1 hour averages) is displayed in Figure 12. Observations started in January 2017, but sample gas was only taken at an inlet height of 5 m for the first 2 months. In March 2017 sampling commenced from the top of the tower (212 m above ground). From August 2017 to November 2017 the lower inlet height was further reduced to 2 m above ground in support of a flux chamber measurement campaign that was carried out at this time.

The expected vertical mole fraction gradient with larger values closer to the surface is directly apparent from the time series (Figure 12). This gradient implies that the area around Beromünster is a net source of N_2O, which is in line with its location in an area intensively used for agriculture (pasture and crop lands). The impact of emissions in the direct vicinity of the tower can also be seen in the enhanced mole fraction variability close to the surface. The by-month standard deviation of the 1-minute observations varied between 0.3 nmol mol^{-1} and 1.6 nmol mol^{-1} for the 5 m inlet height, whereas it remained

below 0.9 nmol mol^{-1} for the 212 m inlet height and was smaller than the one at 5 m in every month. For the 2 m inlet height standard deviations were even larger for the months of August and September 2018 (1.8 and 1.7 nmol mol^{-1}).

Diurnal cycles of the observed N_2O mole fractions at different levels above ground may reveal some of the source and atmospheric mixing dynamics around the tower. On average daytime mole fractions were lower than nighttime observations close to the ground. This feature was observed for almost all months, exceptions being the colder months January, February and March, for which small daytime maxima were observed. Although this agrees with the general process of emission accumulation in more stable, shallow nighttime boundary layers versus increased vertical mixing in more unstable and higher daytime boundary layer, there was considerable variability in the diurnal cycles from month to month that may contain some quantitative information on the seasonality of emissions. It can be suspected that for the winter months, mentioned above, N_2O emissions were not constant over 24 hours, but mainly occurred during the day around and after the time of the observed atmospheric maximum. This could be related to colder nighttime than daytime soil temperatures that suppress N_2O production in the soil. The mole fraction peak in the early daytime hours in March may even hint towards emission bursts from soil freeze/thawing events (Butterbach-Bahl et al., 2013) but may have been caused by local fertilisation events as well. Without local soil and management observations, such interpretations have to remain speculative. In all other months, nighttime mole fractions were larger than daytime mole fractions. The largest day/night differences were observed for the months of August and September 2018. However, at this time observations were done at 2 m instead of 5 m, which makes a direct comparison with other months more difficult. Considerable, but smaller, nighttime increases were also observed from May to June. However, local meteorology and the general advection situation may have been considerably different in these months so that a direct conclusion on the emissions can only remain qualitative and speculative.

At 212 m the diurnal cycles from April to September showed a different pattern than the near surface observations. Mole fractions reached a maximum in the morning hours and decreased again towards the afternoon. This evolution is already well known from CH_4 observations at the same site and was previously interpreted as the upward mixing of more polluted air masses from the stable nighttime boundary layer during the build-up of the convective boundary layer during the morning transition period. In terms of amplitudes by month a similar picture as for the near-surface observations arises with the largest amplitudes being reached in August and September, and lower but similar amplitudes for the months April to July. This again hints that emissions in August and September were larger than in any other month. With a mean diurnal amplitude of 1.4 nmol mol^{-1}, reached in August, the diurnal cycle at 212 m was considerably less pronounced as close to the surface.

The diurnal cycle of the differences between 212 m and near surface observations supports the different levels of nighttime accumulation of N_2O near the surface as discussed above. Nighttime differences were largest in August, September with average values of up to 2.5 nmol mol^{-1} towards the end of the night, whereas the months May to July showed smaller increases in the order of 1 nmol mol^{-1}. The comparison between measurement heights also indicates that in the afternoon hours differences between the two levels become smaller than 0.5 nmol mol^{-1} and were especially small in April. The use of afternoon observations in the inverse modelling is largely justified by this absence of a vertical mole fraction gradient, the vigorous vertical mixing required to sustain this flat profile, and the capability of numerical models to represent this mixing better than the much weaker vertical mixing in the nighttime boundary layer.

Finally, the observations from Beromünster tall tower are compared with those from Jungfraujoch and Schauinsland. The time series reveals that the Beromünster observations at 212 m above ground and those from Schauinsland share very similar N_2O levels and also large parts of their day-to-day variability. Mean baseline mole fractions for Beromünster (212 m) and Schauinsland were 331.5 nmol mol^{-1} and 331.3 nmol mol^{-1}, respectively. Baseline levels at Jungfraujoch were distinctly different from the two other sites, with mean mole fractions of 330.1 nmol mol^{-1}. Variability at Schauinsland was slightly smaller than at Beromünster (212 m), but considerably larger than at Jungfraujoch. The lower variability and lower baseline levels at Jungfraujoch can be attributed to its high-altitude character. The Jungfraujoch time series also contains several N_2O depletion events which are

most likely related to advection of air from the upper troposphere/lower stratosphere that is depleted in N_2O.

In conclusion, this comparison underlines the high quality and good inter-calibration of the new N_2O measurements at Beromünster and shows that they should be suitable for the use in quantitative inverse modeling of N_2O emissions. Furthermore, it documents that atmospheric variability at hourly time scales and at all sites was considerably larger than observation uncertainty, another prerequisite for using the data in quantitative inverse modelling.

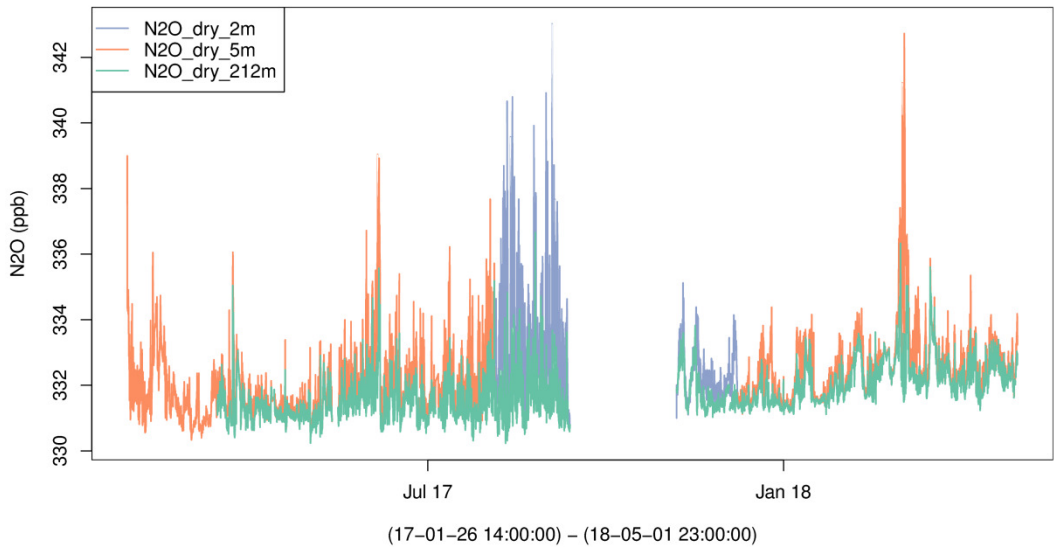

Figure 12: Time series of N_2O observations at Beromünster (1 hour averages) for different inlet heights (colours). Heights are given in metres above ground.

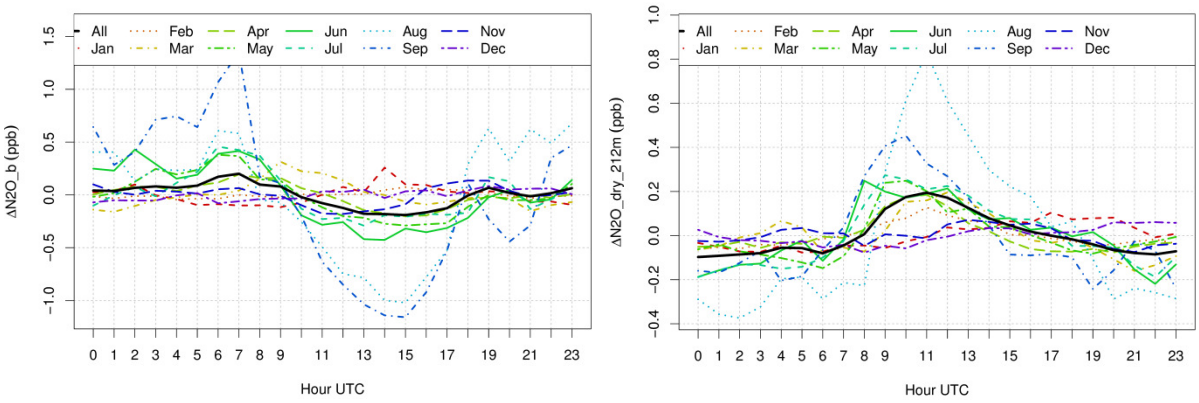

Figure 13: Diurnal cycle by month for the N_2O observations in Beromünster (left) lower inlet height, (right) upper inlet height (212 m). The diurnal cycle was derived as mean hourly deviations from the daily mean. Note that the lower inlet height was usually operated at 5 m, but was lowered to 2 m from August to November 2017.

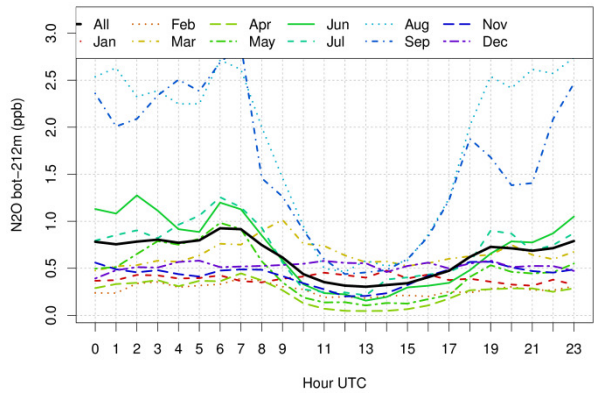

Figure 14: Diurnal cycle by month of the N_2O difference between lower and upper inlet height at Beromünster. Note that the lower inlet height was usually operated at 5 m, but was lowered to 2 m from August to November 2017.

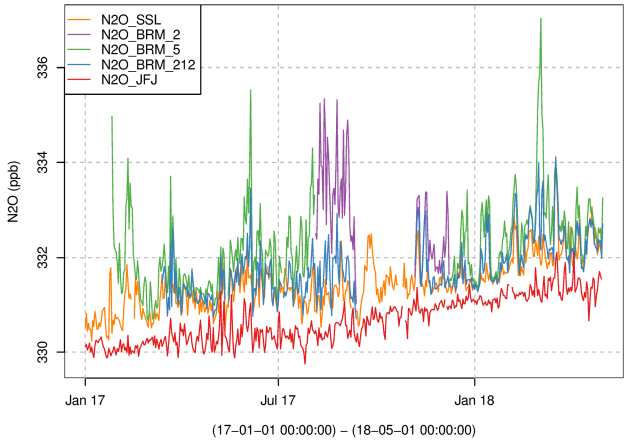

Figure 15: Time series of all N_2O observations used in this study (24 hour averages). Note that only the observations from Beromünster (212 m), Schauinsland and Jungfraujoch were used in the inverse modelling, whereas the observations from the lower inlet heights at Beromünster were not further used.

4 Estimation of Swiss nitrous oxide emissions by inverse modelling

In this section, the results of the inverse modelling experiments are presented. A detailed description of the SI_BASE sector inversion is given in section 4.1 followed by an analysis of different factors of the inversion setup that influence the results (sensitivity inversions) in section 4.2. A summary of all inverse modelling results is provided in section 4.3 together with a comparison with the emissions given in the Swiss NIR. Furthermore, section 4.4 seeks to find explanatory variables for the estimated seasonal variability of the emissions. Finally, a brief discussion of the findings of the current study with results from other European inverse modelling studies concludes this central part of the report.

4.1 SI_BASE inversion results

The observed and simulated N_2O mole fractions for all three sites are shown in Figure 16 for the SI_BASE inversion with low particle release heights. When looking at the performance of the a priori simulations (red) in terms of capturing the observations (black) it becomes immediately apparent that the simulation was largely underestimating the observed variability at Beromünster and Schauinsland in summer, whereas the differences in winter were much less pronounced. It is also apparent that the applied a priori baseline, as derived from the observations at Jungfraujoch, seems to underestimate the real baseline at these sites at all times. This is indicated by the a priori baseline being considerably lower than any of the observations even at times with little variability in the observations, which may indicate relatively unpolluted baseline conditions (e.g., in January 2018 at Beromünster). At the high-altitude site Jungfraujoch, where observed N_2O variability was much smaller than at the lower elevation sites, the a priori simulation was able to reproduce some of the observed pollution events and the a priori baseline followed the lower fraction of the observations sufficiently well, which is not surprising

as it was derived from these. Several negative excursions from the baseline can be seen at Jungfraujoch that were not reproduced by the simulations at all. These may be explained by stratospheric transport events that bring down N_2O-depleted stratospheric air towards Jungfraujoch. Although such transport patterns are in general captured by the transport model, they have no influence on the simulated mole fractions, since only mole fraction changes due to emissions at the surface are evaluated by the model approach, not those due to advection of stratospheric air. Since only a small number of events occurred, their impact on the inverse modelling results should be negligible. In the a posteriori simulations at Beromünster and Schauinsland, the baseline mole fractions were corrected upwards and often agreed well with the lowest observed mole fractions (e.g., January 2018 Beromünster, February 2018 Schauinsland). Hence, the correction seems to be realistic. In section 4.2.6 the influence of the baseline correction onto the inversion results is discussed in more detail. The simulated a posteriori total mole fractions captured the observed levels and variability much better than the a priori simulations. Especially the variability in summer was largely captured by the a posteriori values as well.

This visual impression gained from the inspection of the time series was also confirmed when looking at comparison statistics (Figure 17). The overall and above-baseline correlations between simulations and observations largely improved at all sites from a priori to a posteriori simulations as seen in increases in the coefficient of determination (R^2) for both parameters. At the same time, the RMSE was reduced by more than 40 % at the sites Beromünster and Schauinsland, and by 10 % at Jungfraujoch for a posteriori simulations compared to a priori simulations. These improvements can directly be visualised in a Taylor plot (Taylor, 2001), where for all sites improved Taylor skill scores of the above-baseline signal (TSS_{ea}) were achieved by the a posteriori simulations, with the largest TSS_{ea} being reached at Schauinsland (0.81), followed by Beromünster (0.75) and Jungfraujoch (0.64). The Taylor skill score is defined by

$$TSS = \frac{4(1+R)}{\left(\sigma_f + \sigma_f^{-1}\right)^2 (1+R_0)} \tag{12}$$

where R is the Pearson correlation coefficient between the observed and simulated time series, R_0, here given a value of 0.9, the maximal achievable Pearson correlation coefficient for a perfect simulation, and σ_f the ratio between simulated and observed standard deviations.

Compared with previous CH_4 inversions using observations from the same three sites (Henne et al., 2016), the a posteriori model performance for N_2O was slightly lower in terms of above-baseline R^2, but was similar in terms of TSS_{ea}, the latter resulting from a better performance in terms of simulated variability in the case of N_2O. Very similar results in terms of model performance were obtained from the SI_BASE inversion with high particle release heights. The good model performance can be seen as a proof of concept for the sectorial inversion approach and the general suitability of the N_2O observations and the modelling system.

However, the performance improvement of the a posteriori simulation in itself is no proof of a reasonable inversion performance. In addition to model performance, the χ^2-index, as introduced in section 2.5, can indicate if realistic uncertainties were applied in the inversion. A value close to one can be seen as a minimum test for a well-designed inversion setup. For the SI_BASE inversion χ^2-index took a value of 1.47 (see Table 7), which is reasonably close to one, but may indicate a slight underestimation of both a priori and data-mismatch uncertainties and hence a slight 'over-fitting' of the state vector (interpreting noise as real signal). Sensitivity inversions with optimised covariance parameters that assure a value of the χ^2-index very close to one are discussed in section 4.2.7.

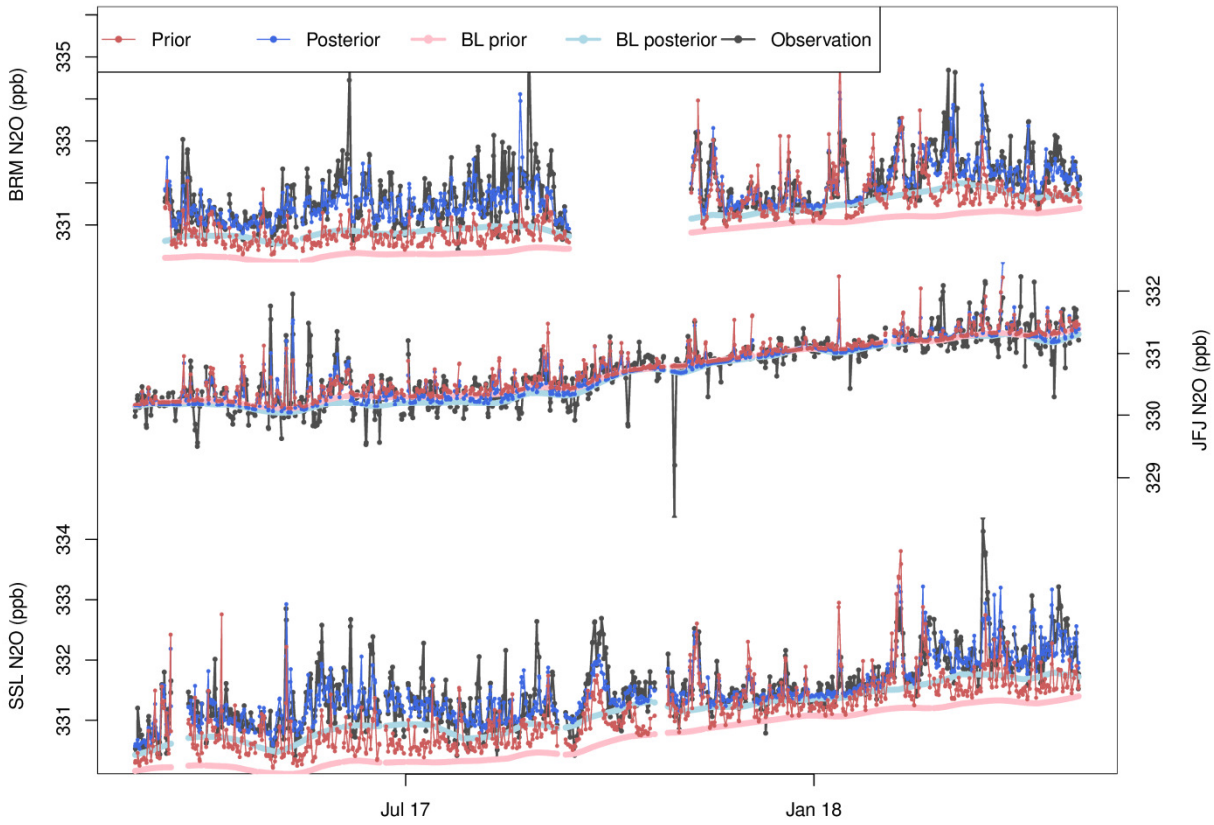

Figure 16: Time series of (black) observed and simulated N_2O mole fractions at the three measurement sites for the SI_BASE inversion with low particle release height. A priori simulations are shown in red, whereas a posteriori values are given in blue. Baseline mole fractions are drawn by thick solid lines using light red and blue accordingly.

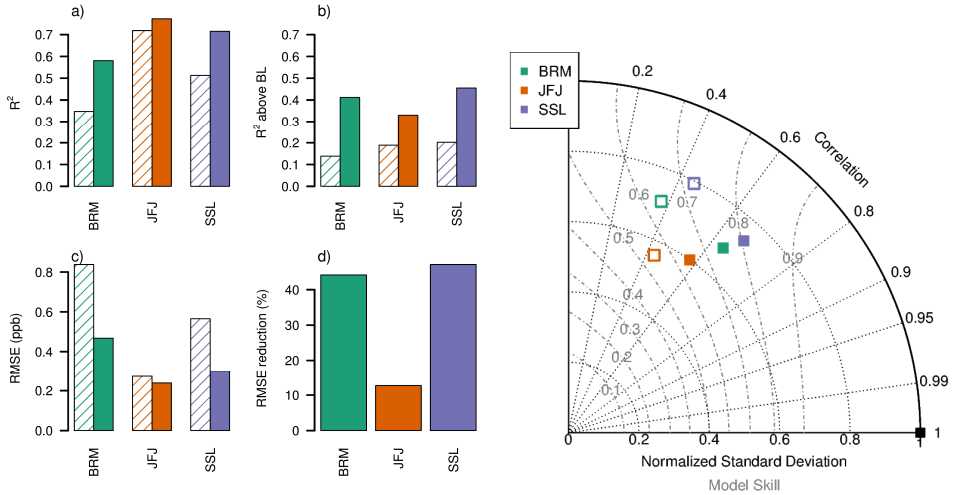

Figure 17: (shaded bars and open symbols) a priori and (solid bars and symbols) a posteriori simulation performance for three measurement sites: a) coefficient of determination for total mole fraction, b) coefficient of determination for above-baseline mole fraction, c) root mean square error (RMSE), d) reduction of RMSE from a priori to a posteriori simulation, e) Taylor plot of above-baseline mole fractions, the gray dashed lines indicated TSS_{ea}.

The annual average Swiss N_2O emissions were estimated by the SI_BASE inversion to be 11.0±0.7 Gg yr^{-1} (1-σ level). This increment compared with the a priori value of 8.9±1.7 Gg yr^{-1} and the latest inventory report of 8.7±1.7 Gg yr^{-1} was mainly due to a posteriori increases in the directAgri (+1.9 Gg yr^{-1}), indirectNat (+0.3 Gg yr^{-1}) and indirectAgri (+0.2 Gg yr^{-1}) sectors (Figure 18). In contrast, emissions in all non-soil emission sectors were lower in the a posteriori results, with the largest absolute changes in the waste sector (-0.12 Gg yr^{-1}). Uncertainty reduction from a priori to a posteriori state varied largely for the different sectors: from >30% for the directAgri to <5% for all non-soil emission sectors. Consequently, the only significant (1σ level) emission increase occurred in the directAgri sector.

Furthermore, an evaluation of the a posteriori covariance structure reveals that considerable negative covariance was obtained between the main emission sector (directAgri) and all other emission sectors (see Figure 19 for a posteriori covariance in central Swiss region; results were very similar for other Swiss regions north of the Alps.). Hence, the lower a posteriori emissions of the non-soil sectors should not be over-interpreted, since they might be a compensatory result of the larger a posteriori emission in the main sectors. However, there seems to be a spatial pattern related to these emission changes that shows lower than a priori emissions in the larger Zurich area, which are also visible in the results of the gridded inversion (see section 4.2.1). Since this region shows neither concentrated agricultural activities nor any large natural ecosystems, the non-soil emission reduction seen by the sector inversion could still be realistic.

The conclusion that not all emissions from all sectors, all regions and at all times can be determined independently by the inversion is also supported by the estimated degree of freedom of the averaging kernel (see section 2.5 for a definition) of this inversion run. The total degree of freedom was 135, meaning that 135 independent pieces of information could be retrieved by the inversion (see Table 7). Of these 135 degrees of freedom, 84 were actually assigned to the emission estimates, whereas the remainder was attributed to the baseline estimation. Even if one assumes that most of this information is put down for the four Swiss emission regions, the degree of freedom still remains much smaller than the 672 unknown emission scaling factors in the Swiss domain (14 months x 4 regions x 12 sectors).

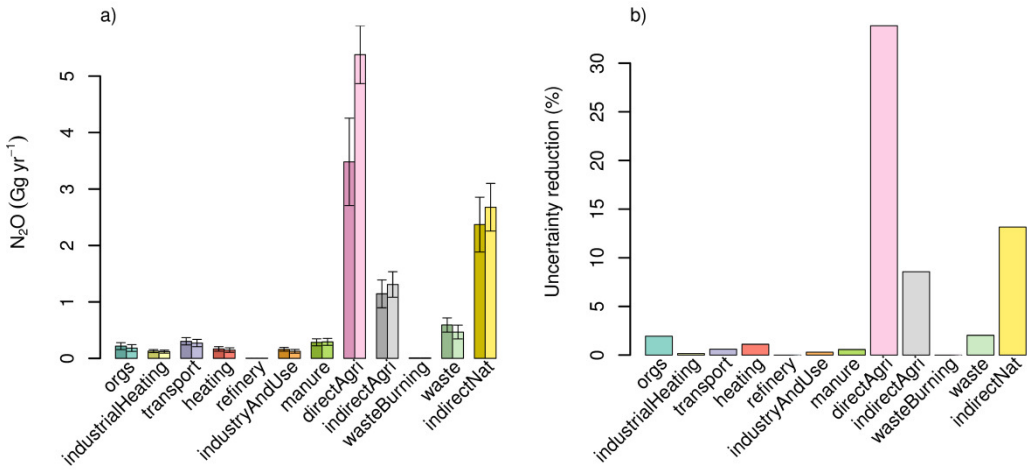

Figure 18: (a) annual mean Swiss N_2O emissions by sector for the SI_BASE inversion with low particle release heights. A priori values are given in darker shade, error bars represent 1-σ uncertainty in each sector. (b) uncertainty reduction $(1 - \sigma_{Ea}/\sigma_{Eb})$ *between a priori and a posteriori emissions.*

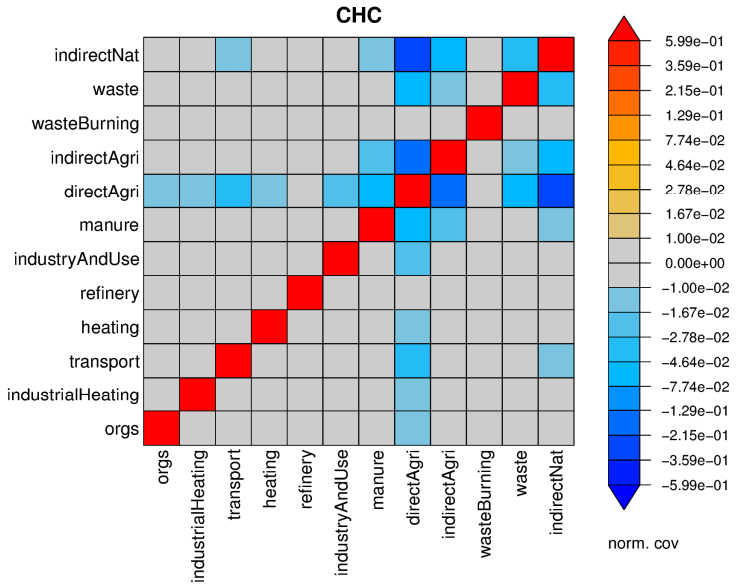

Figure 19: Normalised annual mean a-posteriori covariance structure for the SI_BASE inversion with low particle release heights and the central Swiss region. Large positive or negative off-diagonal values indicate that the emissions of the two respective sources cannot be quantified independently. The matrix was normalised with the values in its diagonal. Note the double-logarithmic scale.

The monthly estimates of the a posteriori N_2O emissions from Switzerland reveal a pronounced seasonal cycle (Figure 20). A posteriori emissions were clearly above the average a priori emissions from May to September and below from October to February. March and April 2017 showed a posteriori emissions at the same level as the a priori. However, in 2018 a posteriori emissions in March and April were generally elevated. Why the a posteriori emissions in these months were so different from one year to the next will be further investigated in section 4.4. The mean summer (JJA) a posteriori emissions were 50 % larger than the annual average, whereas the mean winter emissions were 49 % smaller. Most of the seasonality was introduced by changes in the directAgri, indirectAgri and indirectNat sectors. Other sectors, like manure handling and waste, showed a similar seasonality, but with reduced amplitude as compared to the soil related emission sectors.

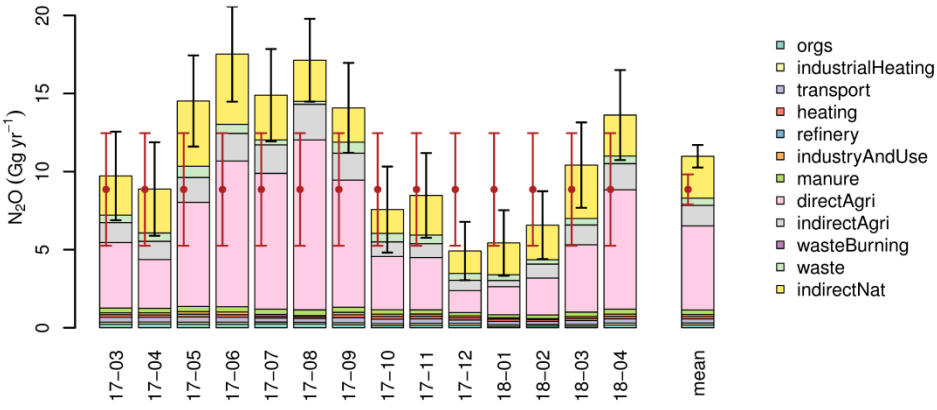

Figure 20: Temporal evolution of monthly mean Swiss N_2O a posteriori emissions and their uncertainties (1-σ level) for the SI_BASE inversion. Red dots and error bars give the a priori emissions and their uncertainties (1-σ level).

Compared to the national total, regional differences existed in the a posteriori adjustments for the different Swiss regions. For the eastern and the central regions (CHE, CHC; see Figure 10) a posteriori differences were actually assigned to the directAgri sector, whereas changes in the other sectors were small in comparison. In the western sub-region (CHW) changes were much less pronounced and even the directAgri sector remained close to the a priori value. However, in the southern part of Switzerland,

the main change was estimated for the indirectNat sector and only smaller positive changes were assigned to the directAgri sector (Figure 21).

These regional differences also become apparent when the a posteriori changes in the regional emission factors are mapped back onto the spatial distribution of the N_2O emissions (Figure 22). On the map, it is clearly visible that a posteriori changes were largest in the central and eastern regions, whereas absolute changes were less pronounced in the west and south. Furthermore, it is interesting to note that the negative a posteriori changes estimated for the non-soil emissions manifest themselves as a negative a posteriori difference in the larger Zurich area but also in other urban areas like Basel, Bern, Lausanne, and Geneva. Adjustments outside Switzerland were much more subtle with the exception of French emissions in the industryAndUse sector, which were strongly corrected downwards, as manifested in the negative a posteriori differences north of Basel in the region of Mulhouse. The reasons for these strong adjustments and the question if they influence the Swiss emission estimates is discussed in section 4.2.8.

The a posteriori results for the SI_BASE inversion with the high particle release showed very similar characteristics as the SI_BASE inversion with the low particle release as discussed here in detail. However, the total annual mean Swiss N_2O emissions for the high release case were 11.5±0.7 Gg yr^{-1}, 0.5 Gg yr^{-1} larger than in the low release case. Furthermore, the amplitude of the seasonal cycle was considerably different for the high release case as well. Summertime and wintertime emissions were only 35 % larger and 38 % smaller than the annual mean, respectively. Surprisingly, summertime emissions were larger for the low particle release case than for the high release.

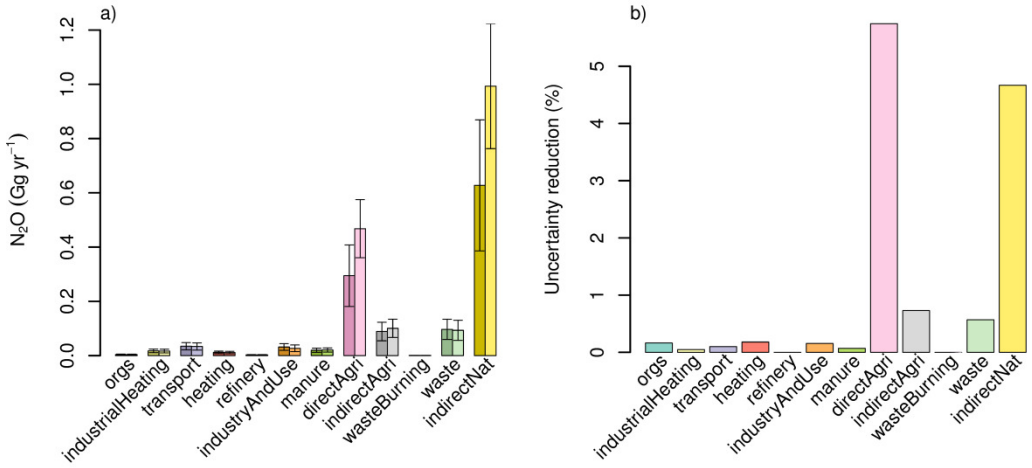

Figure 21: Same as Figure 18 but for southern Switzerland.

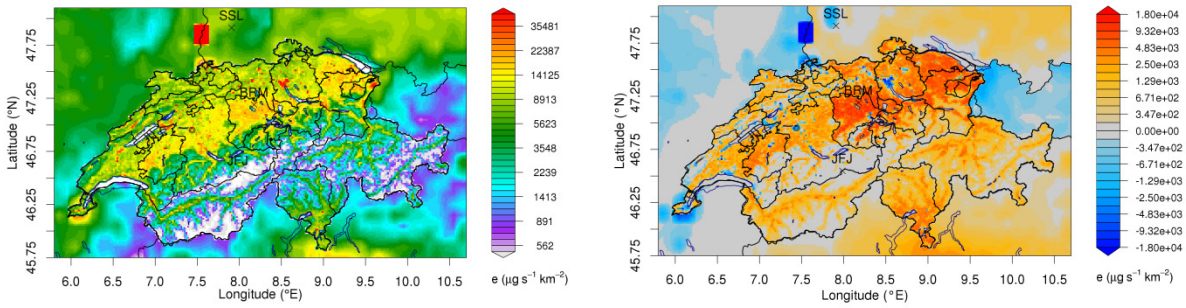

Figure 22: (left) annual mean a priori N_2O emission distribution, (right) annual mean a posteriori minus a priori emissions for base inversion and low model release height (SI_BASE).

4.2 Sensitivity inversions

4.2.1 Gridded inversion

The first sensitivity inversion discussed here is the one based on the gridded inversion system (GI_BASE). Hence, this sensitivity does not test an individual parameter in the inversion setup but rather presents an alternative inverse modelling approach. As discussed above, the gridded inversion was only carried out with a seasonal resolution of the emission fluxes in order to limit the number of unknowns.

As a direct consequence of the reduced resolution grid, considerable spatial aggregation is visible in the a priori emissions of this inversion (Figure 23). This reduced resolution in space and the reduced resolution in time did not impact the a posteriori model performance (TSS_{ea}=0.74 for Beromünster, see Table 7) as compared with the SI_BASE sector inversion. Annual mean a posteriori emission for Switzerland were 8.4±0.5 Gg yr^{-1} and 9.2±0.5 Gg yr^{-1} for the low and high model particle release respectively. This is in close agreement with the a priori values. Spatially, a re-distribution of a posteriori emissions occurred. Emissions in central northern Switzerland tended to be reduced with the exception around Beromünster, but tended to increase in western and eastern Switzerland (Figure 23). The obtained a posteriori pattern does only partly match the one obtained by the sector inversion (Figure 22). Especially the strong a posteriori decreases in the canton of Bern and the lack of an increase in the central area seem to be contradicting features of the two inversions.

The seasonality of national total emissions was slightly reduced as compared with the SI_BASE inversion showing summertime and wintertime emissions 34 % larger and 48 % smaller than the annual average, respectively. Once more these numbers were even smaller for the high particle release case, which showed especially small increases during summer (+25 %). In addition, the spatial allocation of a posteriori emissions varied with season. During spring and fall the patterns were similar to the annual average, whereas in winter widespread emission decreases were estimated everywhere in Switzerland. In contrast, in summer prominent emission increases were estimated in a larger area around Beromünster, western and eastern Switzerland, whereas emission decreases prevailed in the larger Zurich area, along the central northern border and especially in the region around Mulhouse. This pattern is more comparable with that obtained from the sector inversion (SI_BASE), but still estimates much more pronounced a posteriori decreases in the north. The massive a priori emissions around Mulhouse and their strong downward correction by the inversion were already seen by the SI_BASE inversion and are discussed in section 4.2.8 in more detail.

The spatial distribution of a posteriori uncertainty reduction shows reductions of up to 50 % in the direct vicinity of the Beromünster tall tower, whereas for large areas of the Swiss Plateau uncertainty reductions were in the order of 20 % to 40 %. Very little uncertainty reduction was achieved for the cantons of Ticino and Grisons. In addition, very large uncertainty reductions were assigned to the large emissions near Mulhouse, lending trust in the strong a posteriori decreases assigned there. These uncertainty reductions were generally smaller than those achieved by inverse estimates of CH_4 emissions in Switzerland (Henne et al., 2016), which was to be expected due to more challenging observations, expected larger spatio-temporal variability in the emissions and the use of only one measurement site on the Swiss Plateau (in contrast to two for CH_4).

The χ^2-index for the grid inversion was slightly smaller and hence closer to 1 as the one for the SI_BASE inversion. A slightly larger degree of freedom (154) was achieved by the grid inversion. It remains unclear why the two inversion systems, despite these similar performance measures, estimated very different total emissions. Their baseline adjustments were very similar as well, ruling out the introduction of an emission offset (see section 4.2.6). The reduction of the temporal resolution of the emission flux could be one possible reason, but as shown in section 4.2.3, such a reduction in itself did not lead to lower emissions when the sector inversion is used. Another related reason may be seen in the reduced seasonal amplitude; especially summertime estimates were not raised as much as in the SI_BASE and also SI_seas inversions. It could be that the information content per season was still insufficient to adjust the emissions further. A possible source of error, known to sector inversions, is the aggregation to relatively large regions (Kaminski et al., 2001), which may contain variable offsets in the prior fluxes. Since the source sensitivity is not homogeneous within such regions, biased estimates may be introduced. One final reason could be seen in spatial misattribution occurring due to the large a

posteriori corrections north of Basel. However, when using an adjusted a priori with lower emissions in this area (see section 4.2.8), the results for Switzerland are largely unaffected.

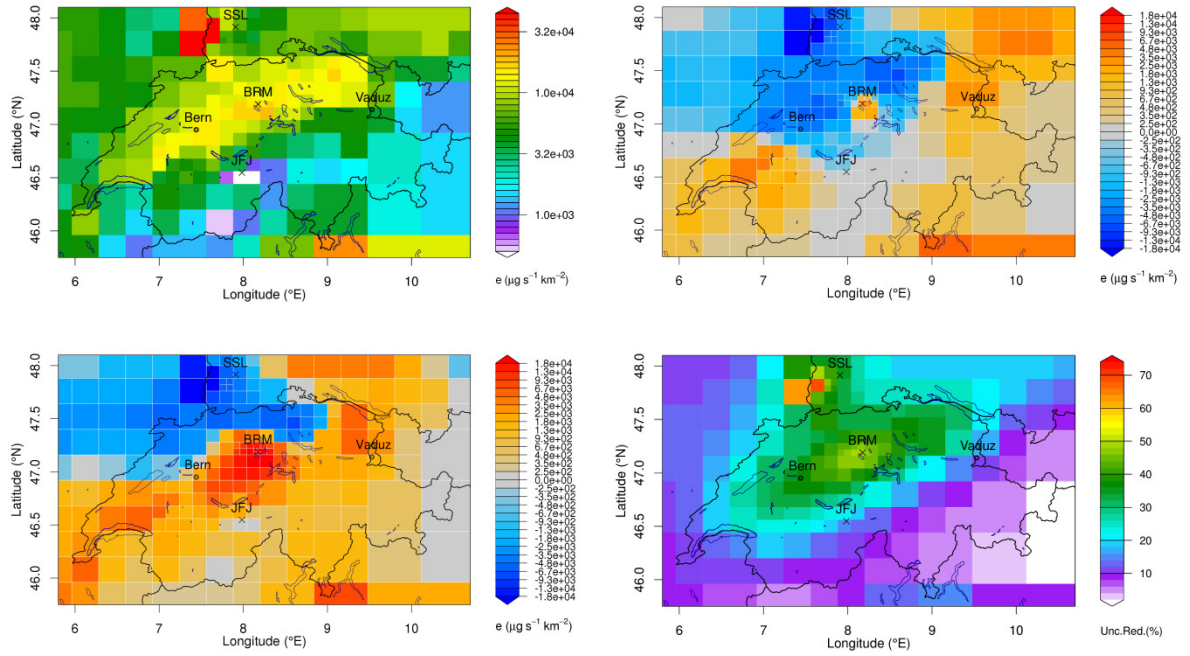

Figure 23: (top left) a priori emissions on reduced inversion grid, (top right) annual mean a posteriori minus a priori emissions, (bottom left) summer (JJA) a posteriori minus a priori emissions, (bottom right) uncertainty reduction $(1 - \sigma_{Ea}/\sigma_{Eb})$ *for gridded inversion seasonal variability of emissions.*

4.2.2 Influence of region definitions

Sub-regions within Switzerland were arbitrarily assigned by cantonal borders and taking general climatological differences into account (north/south of Alps). Other sub-divisions would have been possible. Here, we explore the impact of these choices onto the inversion results. However, this analysis remains limited to a relatively small number of regions in order to keep the size of the inverse problem manageable.

Two additional sensitivity inversion with 3 and 6 Swiss sub-regions were performed. For the first (SI_CH3), two sub-regions of the SI_BASE inversion were joined (CHC and CHE). In the second (SI_CH6), both the CHE and CHW sub-regions of the SI_BASE inversion were further sub-divided following a west-east division (Figure 24).

The total a posteriori Swiss N_2O emissions for both sensitivity inversions remained very close to those of the SI_BASE inversion (Table 7). This was true for the runs with both low and high model particle releases. The a posteriori model performance was virtually the same for these inversions as for the SI_BASE inversion. The use of a smaller (larger) number of regions did only result in marginal decreases (increases) in the number of independent pieces of information obtained by the inversion (DF, Table 7). Hence, one may conclude that there is limited gain from introducing additional sub-divisions to the SI_BAS setup.

Nevertheless, there were some interesting differences when looking at the a posteriori emissions in the different sub-regions. For the SI_CH3 inversions, the results in the sub-regions remained very similar to those in the SI_BASE inversion. This is not surprising, since the two merged sub-regions of the SI_BASE inversion (CHE, CHC) exhibited very similar adjustments. The merged sub-region basically inherited those a posteriori changes. This can also be seen in the spatial distribution of the a posteriori differences that were essentially the same as for the SI_BASE inversion (Figure 25). A further sub-division of the eastern region of the SI_BASE inversion (SI_CH6) had limited effects on the a posteriori emissions in this area. In contrast, a sub-division of the western region resulted in pronounced differences between the new CHWW and CHW regions as compared with the CHW region of the SI_BASE inversion. Especially, a posteriori emissions in the new CHW region were not elevated from the prior

but slightly reduced, whereas the increases in the westernmost sub-region (CHWW) were more pronounced. The resulting a posteriori distribution (Figure 25) shows some features also obtained by the grid inversion (GI_BASE), namely the reduction in the canton of Bern. However, as mentioned before, the national total level of the SI_CH6 inversion was similar to that of the SI_BASE inversion, whereas the one obtained by the grid inversion was considerably lower.

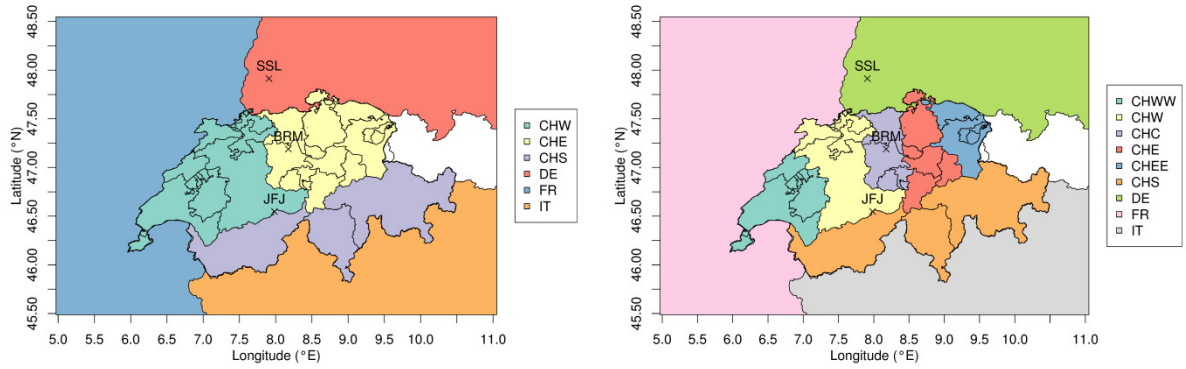

Figure 24: Regional sub-division for sensitivity inversion with (left) 3 Swiss sub-regions (SI_CH3) and (right) 6 Swiss sub-regions (SI_CH6).

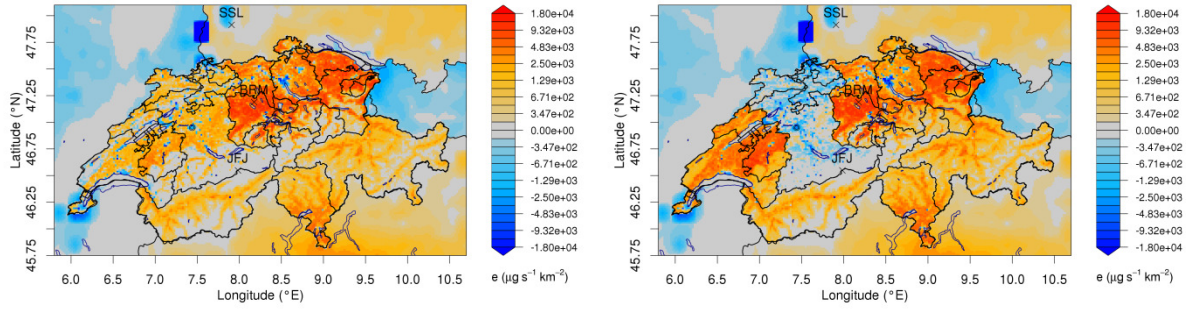

Figure 25: Annual mean a posteriori minus a priori emissions for sensitivity inversions with (left) 3 Swiss sub-regions (SI_CH3) and (right) 6 Swiss sub-regions (SI_CH6) and low model release height.

4.2.3 Influence of temporal resolution of emissions

The grid inversion discussed in section 4.2.1 was run with seasonal resolution of the emissions as compared to monthly resolution of the emissions in the sector inversion. Here, we analyse whether this reduction in temporal resolution may explain the large differences in national total emissions obtained from the two inverse modelling frameworks. To this purpose, the temporal resolution of the sector inversion was reduced to seasonal (SI_seas).

The results of this inversion run remained very similar to those of the SI_BASE inversion. Total national a posteriori emissions were only slightly larger (11.3±0.7 Gg yr^{-1}), and the spatial distribution of a posteriori changes showed the same spatial features as the SI_BASE inversion, see Figure 26. The model performance was only slightly reduced at the Schauinsland site, but remained the same at Beromünster and Jungfraujoch. Also, the seasonal variability remained very similar to that of the SI_BASE inversion, showing average winter-time and summer-time emissions being 55 % smaller and 48 % larger than the annual average a posteriori emissions. Nevertheless, the obtained degree of freedom was significantly lower in the seasonal inversion (84 as compared with 135 in SI_BASE), indicating that the inversion with monthly emission estimates can extract valuable additional information, justifying the monthly approach of the SI_BASE inversion.

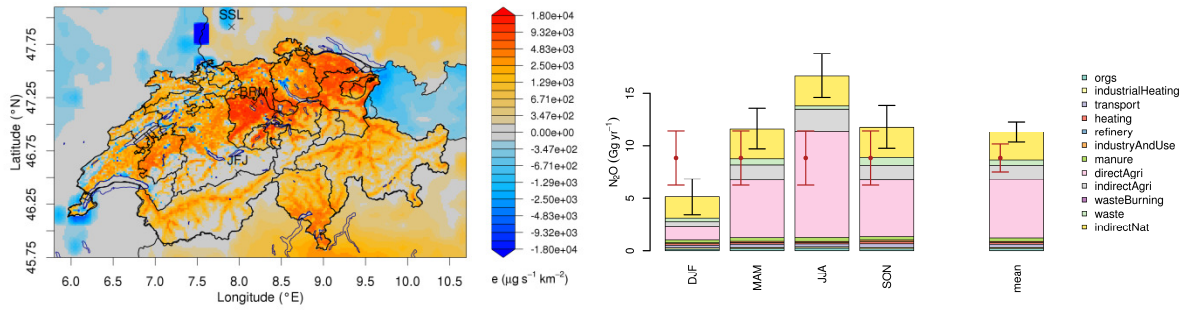

Figure 26: (left) annual mean a posteriori minus a priori emissions and (right) total Swiss emissions by time and sector for sensitivity inversions with seasonal resolution of emissions.

4.2.4 Influence of a priori time profile

In contrast to temporally flat a priori emissions, a sensitivity inversion with a prescribed a priori time profile assigned to soil-related and manure management sectors was carried out (SI_VarPrior). The a priori information was taken from Thompson et al. (2014) for European N_2O emissions.

The temporal variability in the a priori had little impact on the annual mean a posteriori emissions, which remained very close to the SI_BASE estimates (see Table 7) for both inversions with low and high model particle releases. The same is true for the a posteriori model performance and also for the degree of freedom of the inversion.

The a posteriori seasonality was slightly increased in SI_VarPrior as compared with SI_BASE. Mean summer-time and winter-time a posteriori emissions were 65 % larger and 53 % smaller than annual mean a posteriori emissions, respectively. The a posteriori seasonality agreed very well with the a priori values. The largest differences were derived for the months March, May, June 2017 and March, April 2018, all showing larger than a priori emissions in the a posteriori estimates (Figure 27). In this context, it is interesting to note that a shift in seasonality between directAgri and indirectNat N_2O emissions was estimated, with largest indirectNat emissions occurring earlier than those from directAgri. This feature is also present in the SI_BASE inversion, but is more clearly revealed here (Figure 28).

The small differences of this inversion to SI_BASE inversion support the conclusion that the Swiss monthly emissions are well constrained by the observations and additional a priori information is not required to improve the inverse estimates.

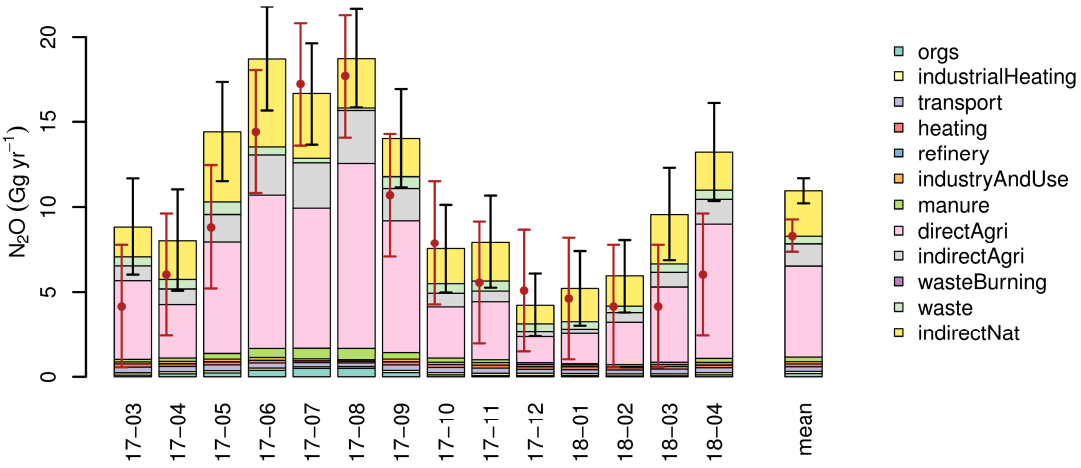

Figure 27: Temporal evolution of monthly mean Swiss N_2O a posteriori emissions and their uncertainties (1-σ level) for the SI_VarPrior inversion and low model particle release. Red dots and error bars give the a priori emissions and their uncertainties (1-σ level).

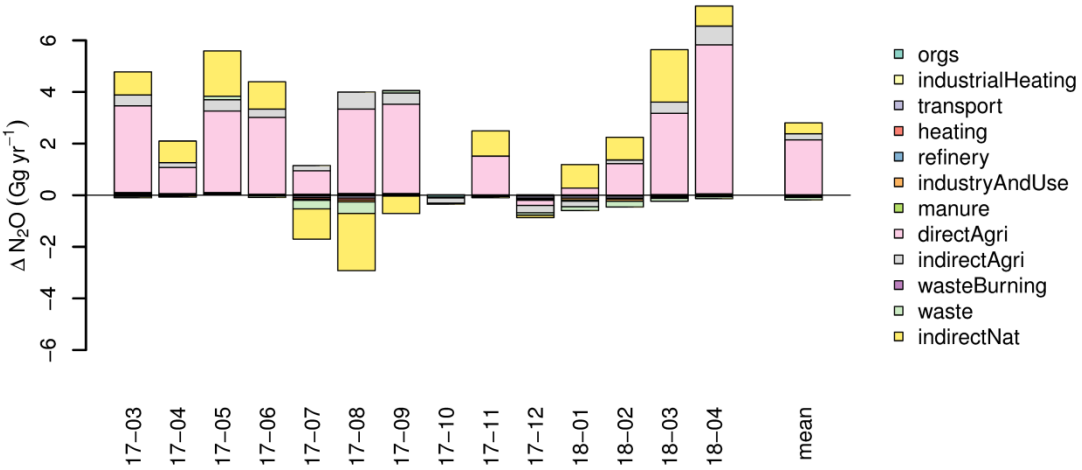

Figure 28: Temporal evolution of monthly mean Swiss N_2O a posteriori minus a priori emissions by sector for the SI_VarPrior inversion and low model particle release.

4.2.5 Influence of a priori uncertainty by sector

In the SI_BASE inversion, the same uncertainties were assigned to each emission sector. According to the Swiss NIR, bottom-up uncertainties differ considerably between sectors, with the largest uncertainties attributed to emissions from wastewater treatment, followed by indirect emissions from soils (Table 4). When using these uncertainties for the a priori uncertainties of the individual sectors in the inversion (SI_SecUnc), slightly different a posteriori results were derived. Although a posteriori national annual mean emissions did not change as compared to SI_BASE, slight shifts between the sectors were estimated. Indirect soil emissions (indirectAgri, indirectNat) were increased more than in SI_BASE, whereas direct agricultural emissions were increased less. As a consequence, uncertainties were reduced more for the former and less for the latter. A posteriori emissions of the waste sector were less corrected than in the SI_BASE inversion, but the relative uncertainty reduction was larger. The latter was mainly due to the larger uncertainty level in the a priori. However, all changes as compared with the SI_BASE inversion remain within the uncertainty estimates of both inversions. Hence, making no additional assumptions on the uncertainty distribution between sectors seems to be justified.

Table 4: Uncertainties assigned to individual emission sectors in the SI_SecUnc inversion. Values according to Swiss NIR (FOEN, 2016).

Category	Uncertainty (%)
orgs	84
industrialHeating	80
transport	34
heating	80
refinery	80
industryAndUse	8
manure	83
directAgri	78.5
indirectAgri	100
wasteBurning	23
waste	164
indirectNat	100

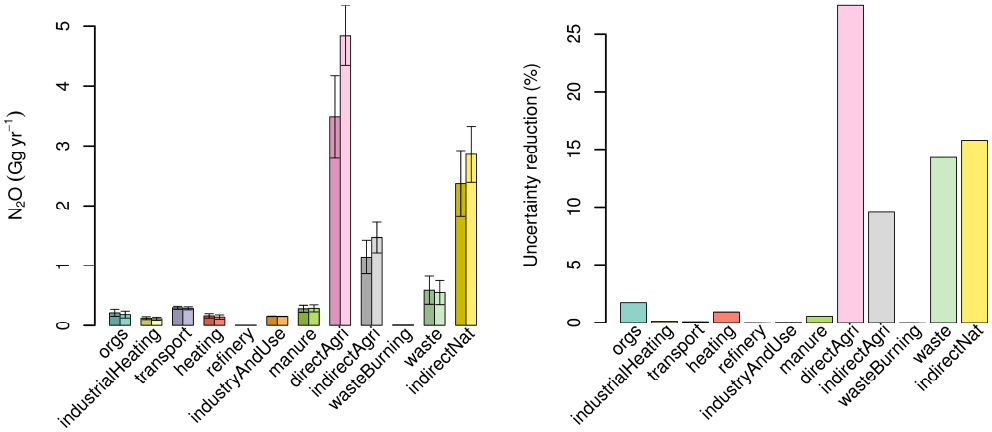

Figure 29: (a) annual mean Swiss N_2O emissions by sector for the SI_SecUnc inversion with low particle release heights. A priori values are given in darker shade, error bars represent 1-σ uncertainty in each sector. (b) uncertainty reduction $(1 - \sigma_{Ea}/\sigma_{Eb})$ *between a priori and a posteriori emissions.*

4.2.6 Influence of baseline uncertainty

From previous inversion studies of CH_4 it became clear that the correct estimation of a realistic baseline is crucial for the determination of the absolute level of the emissions. In general, it can be stated that if the a posteriori baseline is estimated too high (low), less (more) emissions are required to fill the gap between observations and simulations. If the baseline is optimised as part of the inversion (as is the standard approach here), the degree to which the a priori baseline is adjusted critically depends on the uncertainty that was assigned to it. Here, this uncertainty, as the baseline itself, was taken from the REBS fit to the observations at Jungfraujoch. In the SI_BASE inversion and all other sensitivity inversions discussed so far, a value of 0.13 nmol mol^{-1} was assigned to the baseline uncertainty, combined with a temporal correlation length scale of 30 days. Here, alternative inversions with a factor of two lower (SI_uBLlow, GI_uBLlow) and higher (SI_uBLhigh, GI_uBLhigh) baseline uncertainties are presented. The a posteriori baseline was raised compared to its a priori value in the SI_BASE inversions for the two sites Beromünster and Schauinsland. With larger (smaller) uncertainties on the baseline, one can expect that these adjustments will be larger (smaller) for the sensitivity inversions consequently leading to smaller (larger) a posteriori emissions.

This conjecture was confirmed by the sensitivity inversion for both the sectorial and gridded inversion framework. On the one hand, in the low uncertainty case a posteriori emissions were more than 2 Gg yr^{-1} larger than in the base inversions (both grid and sector inversion). On the other hand, a posteriori emissions were at least 1 Gg yr^{-1} smaller for the high baseline uncertainty runs (see Table 7).

A comparison of the a posteriori baseline at Beromünster for all sensitivity inversions with different baseline uncertainties shows that the baseline adjustments were very similar, both in absolute level and in temporal evolution for sector and grid inversion with the same uncertainty level (Figure 32). When evaluating the Swiss a posteriori emissions versus the mean baseline mole fractions for these sensitivity inversions, a clear linear relationship was revealed. For the sector inversion, this relationship had a slope of -11±3 Gg yr^{-1} ppb^{-1}. For the grid inversion, this relationship was a bit less steep (-8.6±3.6 Gg yr^{-1} ppb^{-1}). In general, a posteriori emissions from sector and grid inversion remained at different levels independent of the baseline uncertainty. Hence, other influence factors have to be responsible for this difference, but were not investigated further in this study.

When a posteriori results of all sector inversions are plotted in the same way, it is confirmed that average a posteriori baseline levels are the main influence factor for a posteriori emissions. The only exception is the sensitivity run with optimised covariance parameters (SI_MLoptWoBL) discussed in the next section.

An inspection of the a posteriori time series of the baseline mole fractions reveals that in the high uncertainty runs, simulated baseline mole fraction were frequently larger than the observed mole fractions. For example at Beromünster the times with the lowest (5th quantile) regional contribution to the simulated signal showed an average bias of 0.024 nmol mol^{-1}, which is in contrast to

0.003 nmol mol^{-1} in the base inversion. Though this seems a small difference, it may point towards an exaggerated adjustment of the baseline at least during some periods. In contrast, for the low baseline uncertainty inversions, the simulated baseline mole fractions remained closer to the Jungfraujoch baseline, which lead to a slight underestimation of observed mole fractions at times with very little source sensitivities (e.g., Jan 2018 at Beromünster, -0.045 nmol mol^{-1}).

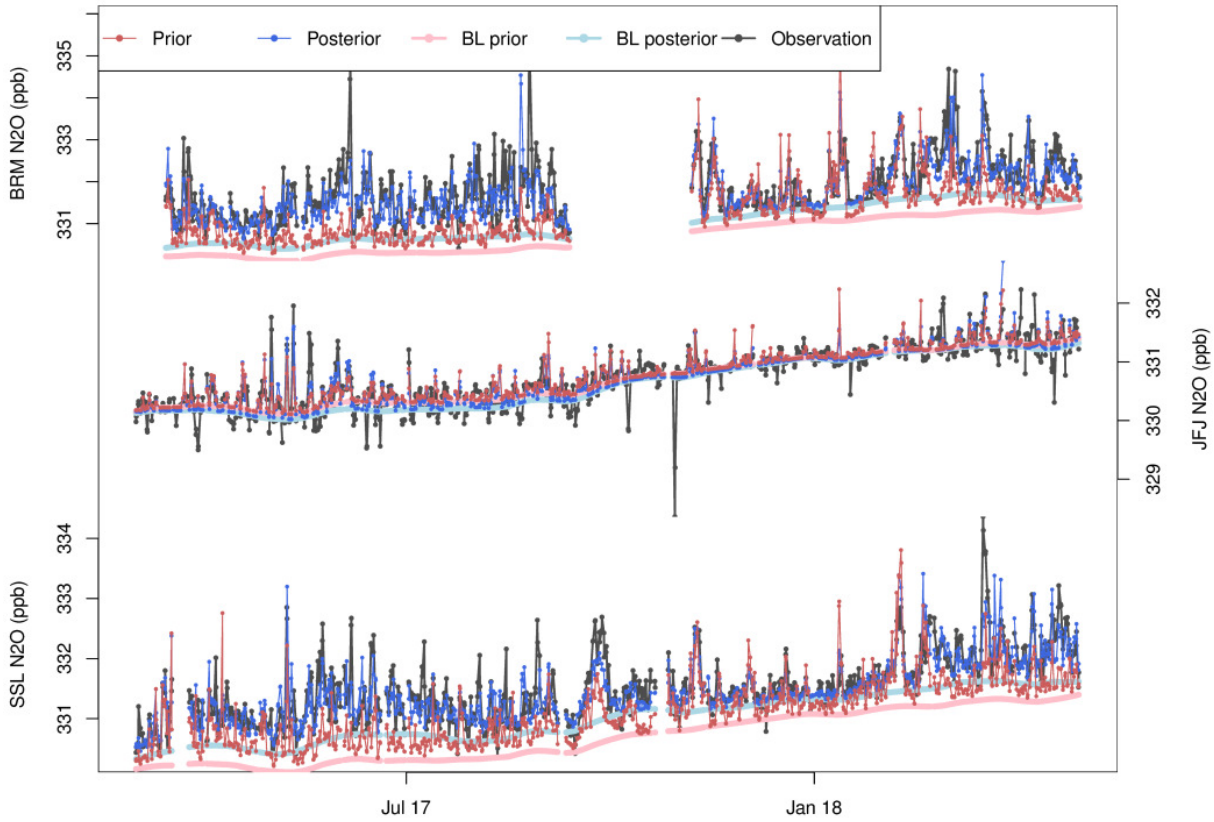

Figure 30: Time series of (black) observed and simulated N_2O mole fractions at the three measurement sites for the SI_uBLlow inversion with low particle release height. A priori simulations are shown in red, whereas a posteriori values are given in blue. Baseline mole fractions are drawn by thick solid lines using light red and blue accordingly.

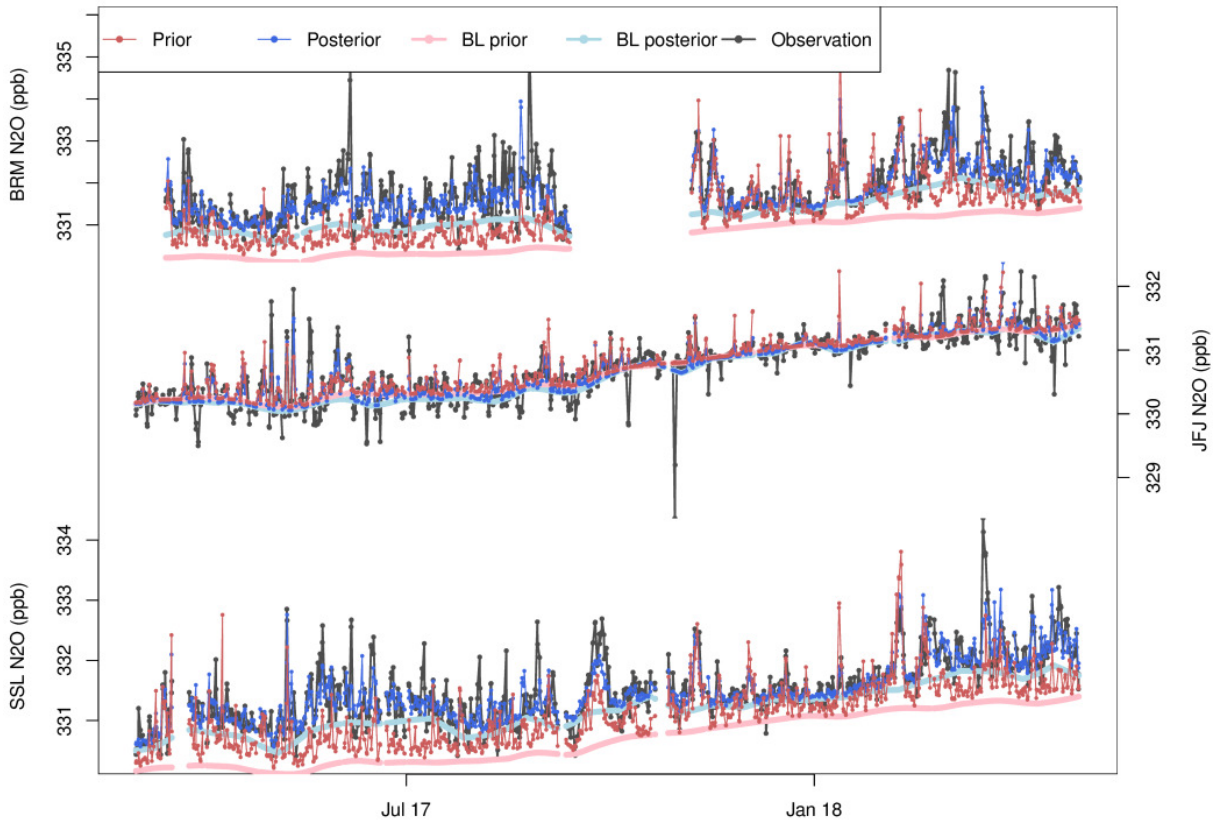

Figure 31: Time series of (black) observed and simulated N_2O mole fractions at the three measurement sites for the SI_uBLhigh inversion with low particle release height. A priori simulations are shown in red, whereas a posteriori values are given in blue. Baseline mole fractions are drawn by thick solid lines using light red and blue accordingly.

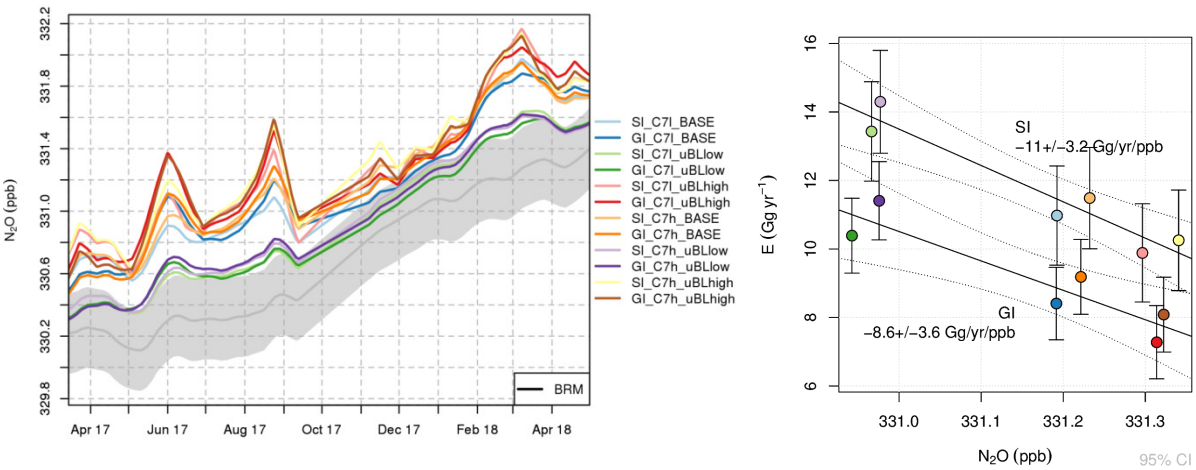

Figure 32: (left) comparison of a posteriori N_2O baseline time series at Beromünster for sensitivity inversions using different a priori baseline uncertainties. The gray line and ribbon give the a priori baseline and its 2σ uncertainty in the SI_BASE inversion. (right) relationship between mean baseline mole fraction at Beromünster and total Swiss N_2O emissions for the same sensitivity inversions. The lines give the results of separate linear fits to the sector and grid inversion runs. Numbers give an estimate of the slope of these fits.

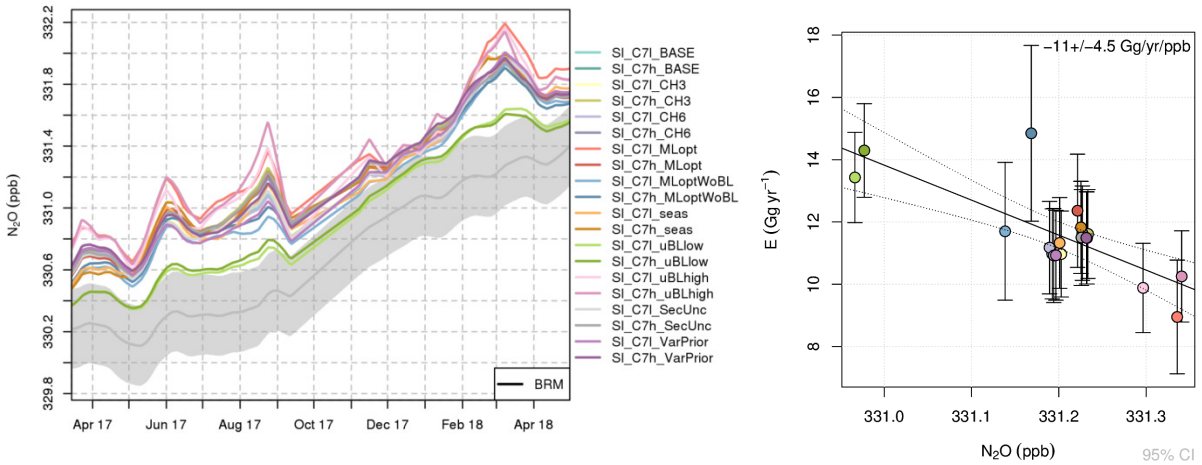

Figure 33: (left) comparison of a posteriori N_2O baseline time series at Beromünster for all sensitivity inversions using the sector approach. The gray line and ribbon give the a priori baseline and its 2σ uncertainty in the SI_BASE inversion. (right) relationship between mean baseline mole fraction at Beromünster and total Swiss N_2O emissions for the same sensitivity inversions. The line gives the results of a linear fit to all sector inversion runs. Numbers give an estimate of the slope of this fit.

4.2.7 Maximum likelihood optimisation of covariance parameters

Two approaches for obtaining more objective parameters describing the covariance matrices were tested. Both are based on likelihood maximisation. In the first case (SI_MLopt) all parameters as described in section 2.5.2 were varied until a maximum in the likelihood estimator was found. In the second case (SI_MLoptWoBL) the set of parameters was limited to those not describing the a priori covariance of the baseline. Results of the parameters obtained in this way are listed in Table 5 and Table 6.

For the parameters describing a priori covariance, the likelihood maximisation largely increased baseline uncertainty at Beromünster and Schauinsland, but also increased the temporal correlation length scale from 30 days to about 80 days. Hence, relatively smooth adjustments to the baseline can be expected when using these parameters in the inversion. In contrast, for Jungfraujoch the baseline uncertainty was strongly decreased. A priori emission uncertainties were optimised on a by-region basis. When optimising both baseline and emission uncertainties, the latter stayed relatively close to their values in the SI_BASE inversion, with the largest changes occurring for the central, southern and eastern Swiss region, whereas smaller emission uncertainties were obtained for the western region. The national total emission uncertainties were 30 % to 50 % larger than in SI_BASE, while the spatial correlation length scale of the a priori emissions stayed very close to the one used in SI_BASE (200 km). When only optimising the non-baseline parameters, the changes in a priori emission uncertainties were amplified reaching values 4 to 5 times as large as SI_BASE in the central region and up to 4 times in the southern region. In addition, a larger spatial correlation length scale of more than 500 km was obtained.

When looking at the parameters describing data-mismatch uncertainty, one can see that the likelihood maximisation resulted, on the one hand, in generally lower σ_{min} for Beromünster and Schauinsland, but on the other hand, larger values of σ_{srr}. In comparison with the SI_BASE inversion, this shift will result in generally lower uncertainties for observations that are linked with low simulated surface sensitivities and vice versa. Potentially this leads to the inversion giving more weight to the low sensitivity observations versus the high sensitivity observations. The latter, however, connected to larger simulated (and observed) mole fractions.

Table 5: A priori covariance parameters as optimised by maximum likelihood approach. Uncertainty estimates are given relative to the values used in the SI_BASE inversion. Baseline uncertainties are given for each site, whereas emission uncertainties are given for each Swiss region.

ID	Relative baseline uncertainty			τ_b	Relative emission uncertainty					L
	BRM	JFJ	SSL	(days)	CHW	CHC	CHE	CHS	CH	(km)
SI_MLopt	3.0	0.4	2.4	84.6	0.8	2.1	1.3	1.4	1.3	205
SI_MLopt	2.7	0.3	2.3	77.2	0.8	2.3	1.8	1.9	1.5	219
SI_MLoptWoBL	1.0	1.0	1.0	30.0	0.9	4.5	0.4	2.3	2.3	537
SI_MLoptWoBL	1.0	1.0	1.0	30.0	1.0	5.8	2.0	3.9	3.2	570

Table 6: Data-mismatch covariance parameters as estimated iteratively in the BASE inversion and optimised with the method of maximum likelihood.

ID	σ_{min} (nmol mol^{-1})			σ_{srr} (-)		
	BRM	JFJ	SSL	BRM	JFJ	SSL
SI_BASE	0.74	0.22	0.48	0.17	0.41	0.20
SI_BASE	0.75	0.22	0.49	0.21	0.41	0.23
SI_MLopt	0.33	0.21	0.24	0.49	0.12	0.27
SI_MLopt	0.30	0.21	0.25	0.61	0.12	0.25
SI_MLoptWoBL	0.36	0.21	0.24	0.42	0.36	0.38
SI_MLoptWoBL	0.33	0.22	0.24	0.56	0.39	0.36

A posteriori results of the two inversions using these optimised covariance parameters differ considerably from those of the SI_BASE inversion. For SI_MLOpt Swiss total N_2O emissions of 8.9±0.9 Gg yr^{-1} were obtained. Although this value was very close to the a priori estimate, considerable spatial and sectorial redistribution of the emissions took place (Figure 34). In the central and eastern Swiss region emissions from directAgri and indirectAgri were raised, whereas emissions from all other sectors were lowered. In the western region all sectors were decreased, but especially those from the directAgri and indirectNat sector. Finally, emissions from the indirectNat sector were strongly raised in the southern sub-region.

In the case of the SI_MLOptWoBL inversion total a posteriori emissions were more similar to the SI_BASE inversion (11.7±1.1 Gg yr^{-1}) for the low model particle release, but were the largest of all sensitivity inversions (14.8±1.4 Gg yr^{-1}) for the high model particle release. The spatial distribution was largely different from SI_BASE, with emphasised emission increases in the central and southern region due to increases in the directAgri and indirectNat sectors, respectively (Figure 34).

For all inversions with optimised covariance parameters, values of the χ^2-index were very close to one, which is in contrast to all other inversions, which showed χ^2-indices larger than 1. This can be seen as a good test but not necessarily sufficient proof of the well-balanced character of the covariance matrices. The obtained degrees of freedom of the MLopt inversions were about 15-20 smaller than for the SI_BASE inversion and most other sector inversions. This difference was more or less proportionally split between emissions and baseline. Together, the comparison of χ^2-index and DF may indicate a slight over-fitting of the observations by the SI_BASE inversion and most other sensitivity inversions.

Overall, the results of the inversions with optimised covariance parameters seem less conclusive than those of the SI_BASE inversion. The large regional differences and large baseline uncertainties, which were accompanied by unrealistic baseline adjustments, seem to contradict the χ^2 test of the covariance parameters. A possible reason for these contradictions could be that the current structure of the covariance matrices, which was prescribed through a small set of parameters, is not sufficiently flexible to capture the real optimal structure these matrices should have. For example, currently only a single parameter for the length scale of the baseline is estimated for all sites. In addition, the uncertainty of

the baseline is constant over time. Both assumptions are probably too limited to describe the true covariance of the baseline. Furthermore, the description of data-mismatch uncertainty as linear function of the total simulated source sensitivity may introduce problems at times when the model does not simulate any emission impact, but the observations show large increases. In this situation, the current approach would assign a small data-mismatch uncertainty, despite the fact that the transport model may have failed to reproduce the emission impact.

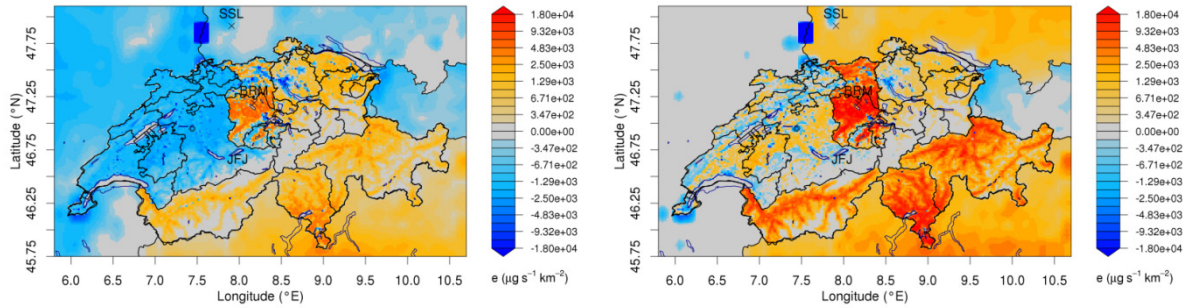

Figure 34: Annual mean a posteriori minus a priori emission differences: (left) for maximum likelihood optimisation of all covariance parameters (SI_MLopt) and (right) for maximum likelihood optimisation of non-baseline parameters (SI_MLoptWoBL), both for low model particle releases.

4.2.8 Influence of large point sources

All inversions showed strongly reduced emissions in the area of Mulhouse, France. For this area, the a priori emissions were taken from the EDGAR inventory. In this inventory, the largest contribution in the area of Mulhouse are attributed to the sector industryAndUse. A comparison with the European Pollutant Release and Transfer Register (E-PRTR, http://prtr.eea.europa.eu/#/home) revealed that two large point sources reporting N_2O emissions are located in the corresponding area. According to E-PRTR, their summed N_2O emissions have changed significantly since the EDGAR reference year (2010), from 2237 t in 2010 to 679 t in 2016 (latest available reporting year in E-PRTR).

In order to analyse if this potentially strongly overestimated source in our a priori has an impact on the Swiss N_2O emission estimates, an alternative set of a priori emissions was compiled. In this set, the EDGAR sector industryAndUse was corrected in the grid cell containing the two point sources from 1.17 ug s^{-1} m^2 to 0.26 ug s^{-1} m^2 according to the values given in E-PRTR. This assumes that no other sources contributed to this sector in the given grid cell. Two inversions (sector and grid) were carried out with the alternative set of a priori emissions. Differences in the derived a posteriori emission were limited to the area close to Mulhouse, where they were about 70 % smaller than in BASE inversions. The influence onto the Swiss domain was limited. For the grid-based inversion, the difference were smaller than 5 % everywhere and total Swiss N_2O emissions remained virtually unchanged. Since this additional test showed no significant differences to the default setup, it was not further included in the set of sensitivity inversions.

4.3 Summary of sensitivity inversions

The results of all sensitivity inversions in terms of annual mean N_2O emissions from Switzerland are summarised in Figure 35. As outlined in the detailed discussions above, a priori baseline uncertainty and to a certain degree a priori emission uncertainties (as varied by the MLopt inversions) were the largest factors impacting mean Swiss emission estimates, whereas the model particle release altitude only had a secondary impact. Systematic differences were also detected between the sector inversion approach and the grid inversion approach. Hence, the ensemble of sensitivity inversions spans a relatively wide range of a posteriori results. Taking the arithmetic mean over all sensitivity inversions displayed in Figure 35 and listed in Table 7, one obtains a value of 10.9±3.4 Gg yr^{-1} for the Swiss N_2O emissions for the period March 2017 to April 2018, which we consider as our best estimate. The uncertainty was calculated as the standard deviation of all sensitivity inversions and was considerably larger than the average over the analytical a posteriori uncertainties (1.4 Gg yr^{-1}). In absolute terms, the overall a posteriori uncertainty was almost the same as the one assigned to the a priori emissions

(±3.5 Gg yr^{-1}). However, in relative terms the uncertainty was reduced to 31 % from a relative a priori uncertainty of 40 %. Due to the remaining large uncertainties, the larger a posteriori emissions cannot be interpreted as being significantly different from the a priori emissions. The difference is only significant at the 27 % confidence level.

The ensemble mean a posteriori emissions by sector (sector inversion only) were very similar to those estimated by the SI_BASE inversion (Figure 36). The largest upward changes as compared with the a priori were assigned to the sectors directAgri, indirectNat and indirectAgri, whereas all other sectors were corrected downward by the inversions. However, increases in indirectNat were slightly more pronounced in the ensemble mean than in the SI_BASE inversion.

The largest uncertainty reductions were also assigned to the three major emission sectors. Ensemble mean seasonality was similar to that in SI_BASE as well. However, the mean seasonal amplitude was somewhat smaller than given by the SI_BASE case with summer (winter) emissions being 40 % larger (43 % smaller) than the annual mean. Seasonality and its drivers will be further discussed in section 4.4. Ensemble mean spatial a posteriori minus a priori differences (Figure 37) were also similar to those of the SI_BASE inversion with the exception of a more pronounced increase in southern Switzerland (indirectNat sector), which shows up as the largest relative change between a priori and a posteriori emissions (Figure 37).

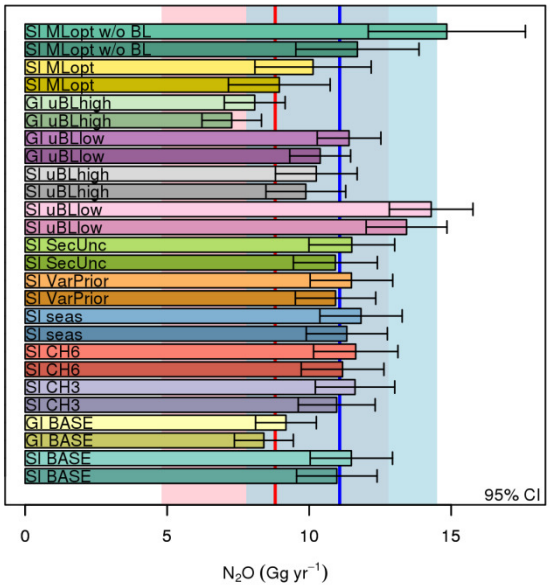

Figure 35: Overview of total Swiss N_2O emission estimates for all sensitivity inversions (labels). The darker (lighter) bars always represent the sensitivity runs using the lower (upper) particle release height in the transport model. The error bars give the individual a posteriori uncertainty (2σ), whereas the thick vertical lines and shaded areas give the average a posteriori (blue) and a priori (red) estimates over all sensitivity inversions.

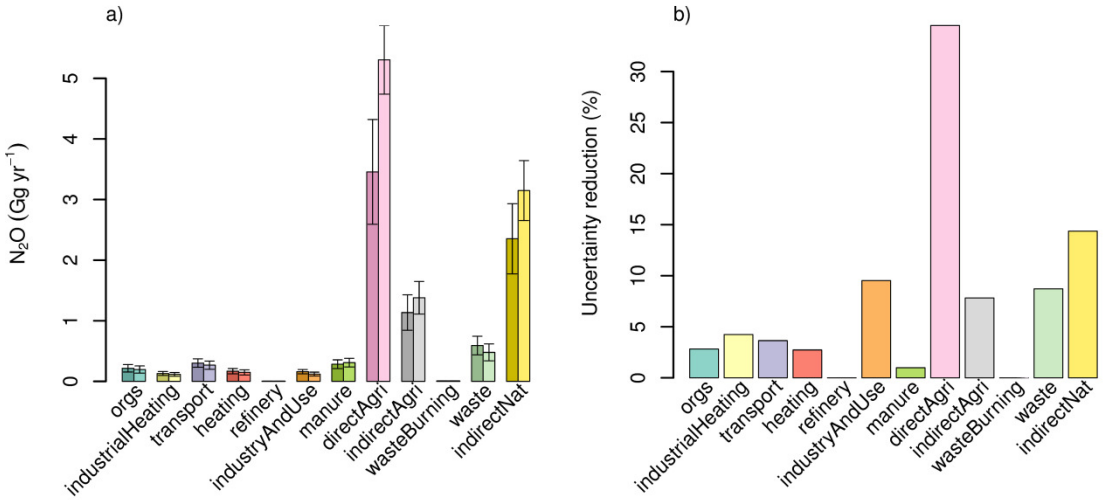

Figure 36: Ensemble mean of (a) Swiss emissions by sector (darker bars: a priori; lighter bars: a posteriori), (b) uncertainty reduction $(1 - \sigma_{Ea}/\sigma_{Eb})$.

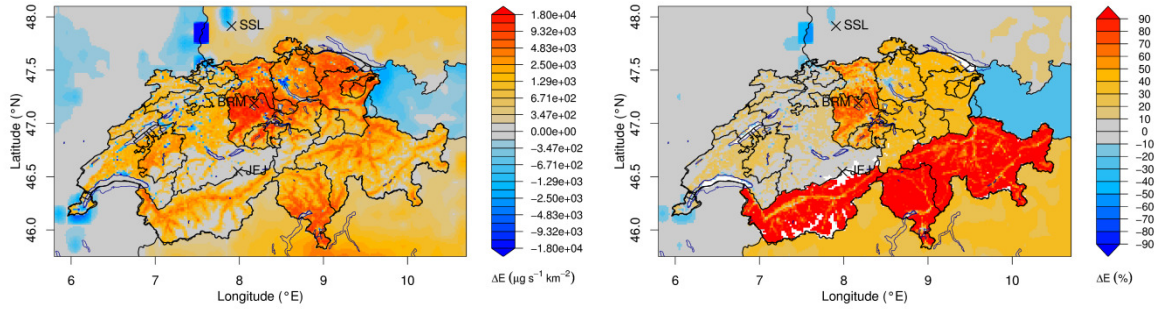

Figure 37: Ensemble mean (all sector inversions) of annual mean a posteriori minus a priori emissions: (left) absolute change (logarithmic scale) and (right) relative change.

Table 7: Overview of results from sensitivity inversions: Swiss annual average N_2O emissions (a priori: E_b;a posteriori E_a, absolute and relative difference), simulation performance against observations (TSS_{ea}), X^2 index, and degree of freedom (DF) of the averaging kernel. Uncertainties are given on 1-σ level.

Inversion Name	Release height	E_b (Gg yr^{-1})	E_a (Gg yr^{-1})	ΔE (Gg yr^{-1})	ΔE (%)	TSSea BRM	TSSea JFJ	TSSea SSL	χ^2-index	DF
SI BASE	low	8.9±1.7	11.0±0.7	2.1	24	0.75	0.64	0.81	1.47	135
SI BASE	high	8.9±1.7	11.5±0.7	2.6	30	0.75	0.65	0.79	1.5	130
GI BASE	low	8.8±1.7	8.4±0.5	-0.4	-5	0.74	0.66	0.8	1.33	154
GI BASE	high	8.8±1.7	9.2±0.5	0.4	5	0.75	0.67	0.79	1.38	149
SI CH3	low	8.9±1.8	11.0±0.7	2.1	24	0.76	0.64	0.81	1.48	131
SI CH3	high	8.9±1.8	11.6±0.7	2.8	31	0.76	0.65	0.79	1.51	125
SI CH6	low	8.9±1.8	11.2±0.7	2.3	26	0.75	0.64	0.81	1.46	140
SI CH6	high	8.9±1.8	11.6±0.8	2.8	31	0.75	0.65	0.79	1.49	134
SI seas	low	8.9±1.8	11.3±0.7	2.5	28	0.76	0.63	0.75	1.5	84
SI seas	high	8.9±1.8	11.8±0.7	3	34	0.75	0.63	0.74	1.52	81
SI VarPrior	low	8.3±1.7	10.9±0.7	2.6	31	0.76	0.65	0.8	1.47	136
SI VarPrior	high	8.3±1.7	11.5±0.7	3.2	38	0.76	0.66	0.79	1.48	130
SI SecUnc	low	8.9±1.8	10.9±0.8	2.1	23	0.76	0.69	0.83	1.47	134
SI SecUnc	high	8.9±1.8	11.5±0.8	2.6	30	0.76	0.7	0.81	1.48	128
SI uBLlow	low	8.9±1.7	13.4±0.7	4.6	52	0.82	0.73	0.86	1.51	110
SI uBLlow	high	8.9±1.7	14.3±0.8	5.4	61	0.83	0.74	0.86	1.51	103
SI uBLhigh	low	8.9±1.7	9.9±0.7	1	12	0.71	0.6	0.77	1.4	157
SI uBLhigh	high	8.9±1.7	10.3±0.7	1.4	16	0.7	0.61	0.75	1.41	150
GI uBLlow	low	8.8±1.7	10.4±0.5	1.6	18	0.81	0.72	0.84	1.28	122
GI uBLlow	high	8.8±1.7	11.4±0.6	2.6	30	0.81	0.73	0.84	1.3	115
GI uBLhigh	low	8.8±1.7	7.3±0.5	-1.6	-18	0.69	0.62	0.76	1.27	175
GI uBLhigh	high	8.8±1.7	8.1±0.5	-0.7	-8	0.7	0.63	0.76	1.31	171
SI MLopt	low	8.9±2.3	8.9±0.9	0.1	1	0.7	0.61	0.72	1.02	117
SI MLopt	high	8.9±2.6	10.1±1.0	1.3	14	0.72	0.62	0.72	1.02	113
SI MLopt w/o BL	low	8.9±4.0	11.7±1.1	2.8	32	0.8	0.73	0.8	1.02	111
SI MLopt w/o BL	high	8.9±5.6	14.8±1.4	6	68	0.83	0.74	0.8	1.02	120

4.4 Relationship between nitrous oxide emissions and environmental controls

Finally, an attempt is made to interpret the large seasonal variability in N_2O emissions, unambiguously determined by most sensitivity inversions, with respect to environmental controls. Figure 38 depicts the ensemble mean normalised seasonal cycle of the most important emission sectors in Switzerland. The largest relative seasonal cycle was estimated for the sectors directAgri and indirectAgri with a clear maximum in August 2018 and a minimum in January 2017. It is interesting to note that the seasonal cycle for the indirectNat sector followed a somewhat different cycle with a reduced amplitude. These emissions reached their maximum in May and June 2017, two months before the maximum occurred for the agricultural soils. The sectors organic soils (orgs) and manure management showed a clear summer emission maximum as well, whereas emissions from wastewater treatment showed a rather unspecific seasonal cycle, with large emissions in May 2017 and some unexplainable variability afterwards. Similar observations can be made for other direct anthropogenic emissions such as those from heating, transport, industrial production and product use. As suggested by the very limited uncertainty

reduction for these sectors (see discussion in section 4.1), their estimated seasonal variability may not reflect true variability but crosstalk from other sectors.

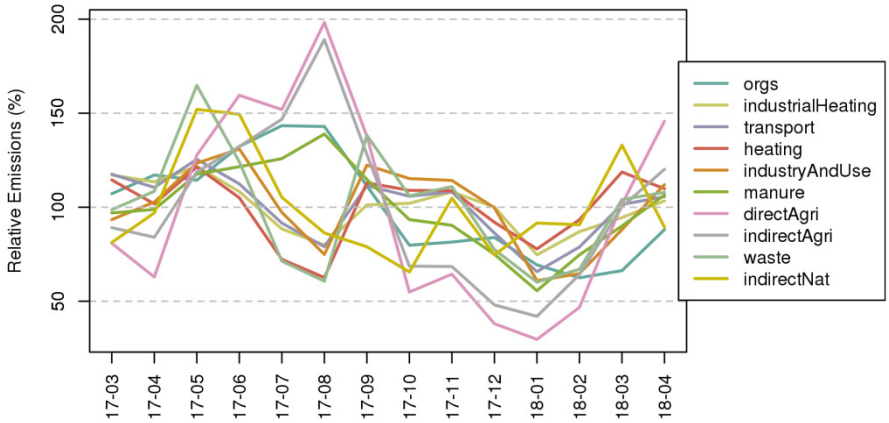

Figure 38: Temporal variability of ensemble mean, a posteriori Swiss N_2O emissions by sector, relative to annual mean. Only sectors that contribute at least 1 % to the Swiss total emissions are shown.

Since the soil-related emission categories (directAgri, indirectAgri, indirectNat) showed the largest seasonal variability and are also the largest contributors to the total Swiss N_2O emissions, it was investigated if their seasonal variability could be directly related to climatological drivers. According to Butterbach-Bahl et al. (2013) N_2O emissions from soils will, among others, depend on management practices, soil temperatures and soil moisture; more specifically on water filled pore space (WFPS), which is a predictor of the efficiency of gas exchange in the soil.

In order to test if a relationship between these predictors and N_2O emissions exists on the scale covered by our inverse modelling results (monthly and country-wide), mean soil temperature and WFPS observations were obtained from the soil observation network of the Swiss Soil Moisture Experiment (SwissSMEX, Mittelbach, 2011; Mittelbach and Seneviratne, 2012). In total, the network consists of 19 sites on different land cover types and different regions of Switzerland. Here, we use the data from 10 grassland sites on the Swiss Plateau, which should best represent soil conditions in the regions with strongest N_2O emissions. Observations of soil temperature and soil moisture at different depths were evaluated (5 cm, 10 cm, 30 cm). From soil moisture observations, water filled pore space was calculated using the soil properties given in Mittelbach (2011). Soil temperatures and WFPS were finally aggregated to monthly means over all sites.

The time series of a posteriori N_2O emissions from soil, soil temperatures and WFPS (Figure 39) reveal a strong common variability between emissions and temperatures. There was little difference in the soil temperatures with depth, whereas WFPS varied with depth showing the largest seasonal amplitude for the uppermost layer.

In the next step, a linear model was constructed to predict N_2O emissions from soil temperatures and WFPS. When only temperatures were considered, the best linear model (largest explained variance, R^2) was obtained when using the 5 cm temperature. This model was able to explain 66 % of the observed variability in the emissions (Figure 40) and the clear positive relationship between temperature and N_2O emissions was confirmed. However, the model still showed large deviations from the linear fit for individual months. For example, the temperature-only model was not able to explain why emissions in the months March and April were distinctly different for 2017 and 2018 (blue dashed line in Figure 39 top). When building a multi-linear model combining temperature and WFPS effects, the best model was again obtained when using the 5 cm observations. The combined model was able to explain 86 % of the observed emission variability and reduced the model RMSE from 2.2 Gg yr^{-1} to 1.4 Gg yr^{-1} (Figure 41). Although difficult to see directly in the time series plots, the dependency of N_2O emissions on WFPS was positive when temperature dependency was considered in the same model. A positive correlation of N_2O emissions and WFPS is well established for the range of WFPS values covered here (Butterbach-Bahl et al., 2013). N_2O emissions are expected to decrease only for very large values of WFPS close to 100 %. The differences in March/April emissions between 2017 and 2018 were mostly

explained by the combined model, which largely attributes the increased emissions in 2018 to larger WFPS (March) and soil temperature (April).

Freeze/thaw cycles at temperatures around 0°C were speculated to lead to intense pulses of N_2O releases from soils, possibly acting as a significant source in the annual budget (Butterbach-Bahl et al., 2013). On the scale investigated here, the temperature-emission relationship did not show any signs of increased N_2O emissions during freeze/thaw conditions as could be suspected for the months with lowest soil temperatures. Either these freeze/thaw cycles only enhance emissions at very short time intervals (emission bursts) and are averaged out in the atmospheric observations and our inverse modelling approach, or the winter 2017/2018 did not feature the required conditions. The latter seems possible since the winter was relatively mild for the Swiss Plateau and temperatures were above average for extended periods (MeteoSwiss, 2018).

It may be debated if temperature is the real forcing of N_2O emissions or if it is only a proxy for management, which, due to a lack of statistical data, was not taken into account here. Warmer temperatures implicate increased management of agricultural soils in terms of fertiliser and manure application and, hence, increase the amount of available nitrogen compounds in the soils. This consideration is supported by the different seasonality observed for N_2O emissions from (semi-)natural ecosystems. These do not correlate as well with temperatures as do those from agricultural soils. Furthermore, regional differences in the seasonality of the emissions were obtained by the inversion. For individual regions, the linear relationship to the soil observations was not as pronounced. This may be due to increased uncertainties in the regional emission estimates or the soil observations being less representative for mean soil conditions on a by-region basis.

Overall, one may conclude that the strong relationship between well-known environmental controls of N_2O emissions from soils and the inverse emission estimates confirms the successful application of the inversion framework and the feasibility of such inversion studies on the Swiss scale. The relationship was established on a rather long time (month) and spatial (order of 100 km) scale. Locally, N_2O emissions will depend on other, more immediate factors as well.

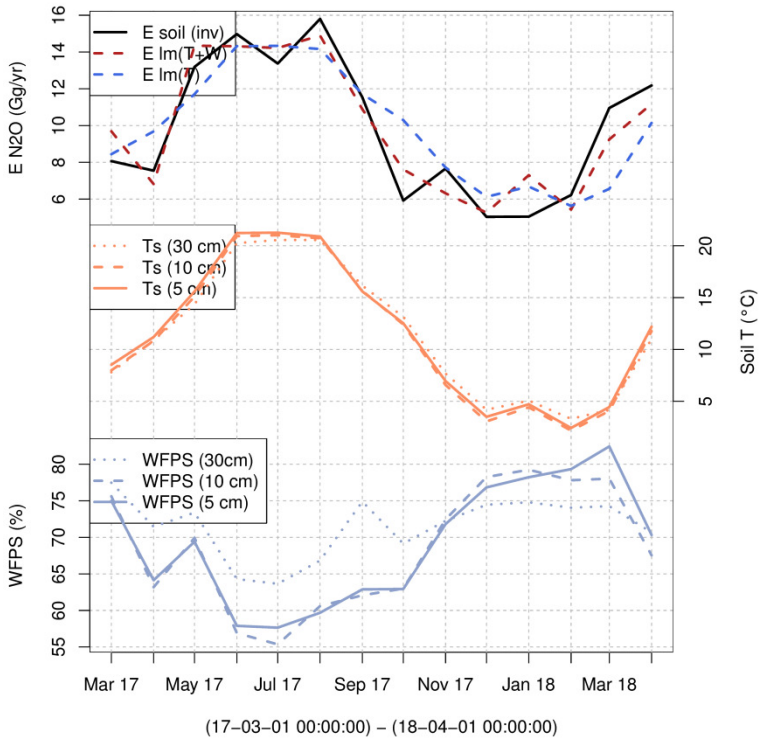

Figure 39: Time series of (top, black line) ensemble mean monthly Swiss N_2O emissions from soils as estimated by inverse modelling and (blue and red dashed lines) linear model predictions (see text for details). (middle) mean soil temperatures and (bottom) mean water filled pore space (WFPS) at Swiss grassland sites and different soil depths.

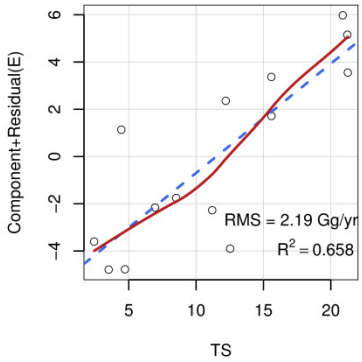

Figure 40: Partial-residual plot for linear model based on temperature (TS) only.

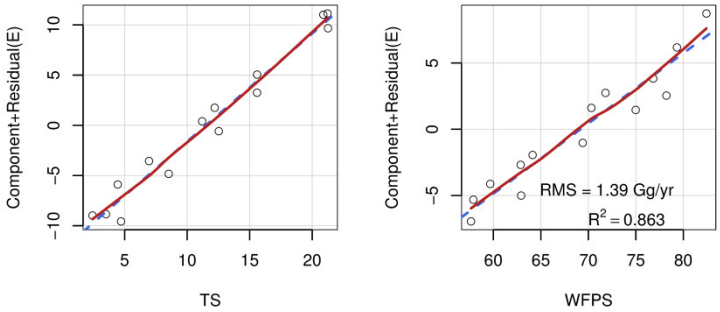

Figure 41: Partial-residual plots for linear model based on (left) soil temperature (TS) and (right) water filled pore space (WFPS).

4.5 Discussion of previous top-down estimates of N_2O emissions in Europe

Several previous studies have used inverse methods to derive N_2O emissions on the European and national scale. As part of the EU-FP7 INGOS project, four different inverse modelling systems were applied at the European scale (Bergamaschi et al., 2015). Their a posteriori estimates for the period 2006 to 2013 indicated larger emissions than reported to the UNFCCC and also larger than those included in EDGAR for the EU-28 region (Bergamaschi et al., 2018). However, most inverse estimates were within the large uncertainty margins reported to the UNFCCC (~±100 %). On the EU-28 scale, indirect emissions from (semi-)natural ecosystems were considered small and were not thought to account for the differences between bottom-up and top-down estimates.

On the national scale, N_2O emissions were estimated for the UK and Ireland by Ganesan et al. (2015) and also reported as an annex to the UK NIR (Brown et al., 2018). These validation studies included in the UK NIR show good agreement between bottom-up and top-down estimates within their associated uncertainties and for the complete reporting period from 1990 onwards. However, as for the European scale validations study, top-down estimates were slightly larger than values reported in the NIR. The study by Ganesan et al. (2015) covered a much shorter period (2012 – 2014) and estimated annual mean emissions of 100 Gg yr-1 for the UK, which is in close agreement to the bottom-up estimates in the NIR for the same period. Both Ganesan et al. (2015) and NIR report considerable seasonality in the emissions. These are in a very similar range (+50 % in summer, -50% in winter) as obtained in this study for Switzerland.

5 Summary and conclusions

With the N_2O observations started in March 2017 at the tall tower Beromünster and the new, spatially distributed N_2O emissions inventory compiled for this project, it was possible to assess the total Swiss N_2O emissions with independent top-down methods for the first time. Despite the challenges posed in terms of required measurement precision and in terms of expected spatial and temporal variability in the N_2O emissions, this study proves that it is in general possible to retrieve N_2O emissions on the scale of a small country by adequate atmospheric observations and inverse modelling.

The best estimate of Swiss total annual N_2O emissions, as derived in this study for the period March 2017 to April 2018, was 10.9±3.4 Gg yr^{-1}, which compares to 8.7±3.5 Gg yr^{-1} given in the Swiss NIR for 2016 (FOEN, 2018) and similar to the a priori information used for the inverse modelling. Due to the large uncertainties connected to both numbers, these estimates are only different on a 27 % confidence level. The relative uncertainty of the inverse modelling estimate (31 %) was smaller than that of the NIR estimate (40 %), whereas the absolute uncertainties were not reduced by the inverse modelling. The relatively large uncertainty range of the inverse modelling results was calculated from the spread over a set of 26 sensitivity inversions. These sensitivity tests comprised the application of two different inversion approaches: one focussing more on the spatial distribution (grid inversion), the other on the temporal evolution and emissions by sector (sector inversion). Further uncertainties in the inversion setup were explored by varying some of the important influence factors like a priori uncertainties and region definitions. The largest contributors to the a posteriori spread were the definition and uncertainty of a baseline mole fraction required by the model approach, and unexplained differences between grid and sector inversion.

Most of the differences seen by the inversion in the national total emissions were assigned to higher than a priori direct emissions from agricultural soils (central and eastern Swiss Plateau) and to a smaller degree to higher indirect emissions from natural (southern Switzerland) and agricultural soils, whereas lower than a priori emissions were assigned to more direct anthropogenic emission sectors (transport, heating, wastewater). However, the changes in these minor emission sectors were associated with larger uncertainties and considerable negative covariance towards the major emission sectors. Hence, it cannot be concluded that they are significant. Nevertheless, lower than a priori emissions were also assigned to the Zurich urban area by the grid inversion, suggesting that overall N_2O emissions in urban areas may be overestimated in the NIR. Another possible reason for the larger than a priori emissions obtained by the inversion could be the neglect of natural N_2O emissions in the a priori inventory. These are also not included in the NIR, but may account for 1.37 Gg N_2O yr^{-1} (Bühlmann, 2014), a considerable fraction of the observed discrepancy.

All inversions produced a pronounced seasonality in the emissions with a mean amplitude over all inversions of ±40 % of the annual mean. Largest emissions were estimated in summer, smallest in winter. However, there was considerable spread in the seasonality as well, with the tendency of inversions with smaller annual total emissions to predict smaller summertime emissions and as a consequence also a smaller seasonal amplitude.

As expected, the seasonality was dominated by emissions from soils. It was possible to link the month-to-month variability in soil emissions to two environmental controls (soil temperature and soil water filled pore space), which together were able to predict 86 % of the observed variability and could also explain pronounced year-to-year differences for emissions in March and April. The tendency to larger than reported N_2O emissions obtained here for Switzerland compares well with other recent studies estimating N_2O emissions in Europe with similar inverse modelling approaches. Both on a by-country as well as on the European scale, inverse estimates were usually larger than emissions reported to the UNFCCC and estimates of the EDGAR inventory. Some of these studies also highlight a similarly pronounced seasonality as obtained in this report. All this lends additional credibility to the findings of this study and are encouragement to continue with the observations and inverse modelling of N_2O emissions in support of the NIR.

6 Outlook

The present study underlines the general feasibility of inverse modelling of Swiss N_2O emissions using atmospheric observations from the Beromünster tall tower on the central Swiss Plateau. Although robust estimates of the national total N_2O emissions were derived, these varied considerably between different sensitivity inversions and especially by the applied inversion method and the applied baseline mole fractions. Nevertheless, it was possible to reduce the relative emission uncertainty from around 40 % in the Swiss NIR to about 30 % in this study.

Future inverse modelling studies will need to further improve this number. This may be achieved by improvements in the inversion modelling setup. For example, including baseline mole fractions from a global scale N_2O transport model, ideally unbiased, could improve the large uncertainty currently

introduced by using a baseline derived from observations at Jungfraujoch. Furthermore, a re-evaluation of the region and sector definitions as used in the current sector inversion may be beneficial. It was shown that for most of the minor emission sectors only limited independent information could be gained from the inversion. A different re-grouping of emission sectors may help to gain further insights. For example, one could disconnect region and sector definition as it was used here and instead use different regional definitions for different sectors (e.g., several sub-regions for the main emission sector (direct agricultural), but only one or two regional factors for minor emission sectors like transport or heating for which little regional differences can be expected).

The inverse modelling results should further be analysed in terms of environmental controls, direct emission flux measurements (coming either from long-term studies or from campaigns), and comparisons with soil process models. This may further improve the understanding of soil related N_2O emission fluxes and also help to improve process models and management practices to avoid excessive N_2O emissions in the future. This may especially be interesting in light of the extremely dry and warm summer 2018, for which the N_2O inversion was not yet carried out.

Last but not least, it is absolutely crucial for the future of inverse modelling of Swiss N_2O emissions that the observations at Beromünster tall tower are continued with the high quality outlined in this report. Without these observations and relying only on those from Jungfraujoch and Schauinsland, N_2O emission estimates on the Swiss scale are bound to fail. The current observations and inverse modelling will be continued within the framework of the FOEN project CLIMGAS, which will also comprise inverse modelling of CH_4. Inverse modelling of halocarbons on the Swiss scale is currently foreseen in an SNF-funded project (IHALOME), including new observations at Beromünster. If these observations and modelling efforts are successful, a top-down assessment of most non-CO_2 GHG emissions in Switzerland can be achieved.

Acknowledgements

The following people were involved in setting up and maintaining the N_2O observations at Beromünster: Patrik Zanchetta, Simon Wyss, Erkan Ibraim, Beat Schwarzenbach, Thomas Bruggisser. Calibration standard gases were prepared and calibrated against NOAA standards by Christoph Zellweger and Simon Wyss at Empa. N_2O data from Schauinsland were provided by Frank Meinhardt, UBA. SwissSMEX soil observations were provided by Sonia Seneviratne, ETH Zurich. COSMO-7 analysis fields were generated and made available by MeteoSwiss.

References

Berchet, A., Pison, I., Chevallier, F., Bousquet, P., Conil, S., Geever, M., Laurila, T., Lavrič, J., et al.: Towards better error statistics for atmospheric inversions of methane surface fluxes, Atmos. Chem. Phys., 13, 7115-7132, doi: 10.5194/acp-13-7115-2013, 2013.

Bergamaschi, P., Corazza, M., Karstens, U., Athanassiadou, M., Thompson, R. L., Pison, I., Manning, A. J., Bousquet, P., et al.: Top-down estimates of European CH_4 and N_2O emissions based on four different inverse models, Atmos. Chem. Phys., 15, 715-736, doi: 10.5194/acp-15-715-2015, 2015.

Bergamaschi, P., Danila, A., Weiss, R. F., Ciais, P., Thompson, R. L., Brunner, D., Levin, I., Meijer, Y., et al.: Atmospheric monitoring and inverse modelling for verification of greenhouse gas inventories, Publications Office of the European Union, Luxembourg, ISBN 978-92-79-88938-7, doi: 10.2760/759928, 2018.

Brown, P., Broomfield, M., Cardenas, L., Choudrie, S., Kilroy, E., Jones, L., MacCarthy, J., Passant, N., et al.: UK Greenhouse Gas Inventory 1990 to 2016: Annual Report for submission under the Framework Convention on Climate Change, Department for Business, Energy & Industrial Strategy, 860, 2018.

Bühlmann, T.: Durch Stickstoffdeposition induzierte Emissionen von Stickoxiden und Lachgas aus (semi-)natürlichen Ökosystemen, BAFU/FOEN, 40, 2014.

Bühlmann, T., Hiltbrunner, E., Körner, C., Rihm, B., and Achermann, B.: Induction of indirect N2O and NO emissions by atmospheric nitrogen deposition in (semi-)natural ecosystems in Switzerland, Atmos. Environ., 103, 94-101, doi: 10.1016/j.atmosenv.2014.12.037, 2015.

Butterbach-Bahl, K., Baggs, E. M., Dannenmann, M., Kiese, R., and Zechmeister-Boltenstern, S.: Nitrous oxide emissions from soils: how well do we understand the processes and their controls?, Philosophical Transactions of the Royal Society B: Biological Sciences, 368, doi: 10.1098/rstb.2013.0122, 2013.

Daelman, M. R. J., van Voorthuizen, E. M., van Dongen, U. G. J. M., Volcke, E. I. P., and van Loosdrecht, M. C. M.: Seasonal and diurnal variability of N2O emissions from a full-scale municipal wastewater treatment plant, Science of The Total Environment, 536, 1-11, doi: 10.1016/j.scitotenv.2015.06.122, 2015.

FOEN: Switzerland's greenhouse gas inventory 1990-2014, Submission of April 2016 under the United Nations Framework Convention on Climate Change and under the Kyoto Protocol, Federal Office for the Environment (FOEN), Bern, 2016.

FOEN: Switzerland's greenhouse gas inventory 1990-2016, Submission of April 2018 under the United Nations Framework Convention on Climate Change and under the Kyoto Protocol, Federal Office for the Environment (FOEN), Bern, 2018.

Ganesan, A. L., Manning, A. J., Grant, A., Young, D., Oram, D. E., Sturges, W. T., Moncrieff, J. B., and O'Doherty, S.: Quantifying methane and nitrous oxide emissions from the UK and Ireland using a national-scale monitoring network, Atmos. Chem. Phys., 15, 6393-6406, doi: 10.5194/acp-15-6393-2015, 2015.

Henne, S., Brunner, D., Oney, B., Leuenberger, M., Eugster, W., Bamberger, I., Meinhardt, F., Steinbacher, M., et al.: Validation of the Swiss methane emission inventory by atmospheric observations and inverse modelling, Atmos. Chem. Phys., 16, 3683-3710, doi: 10.5194/acp-16-3683-2016, 2016.

Henne, S., Brunner, D., and Emmenegger, L.: Quantifizierung der Schweizer Methanemissionen mittels atmosphärischer Messungen und inverser Modellierung, Empa/BAFU, Dübendorf/Bern, Switzerland, 52, 2017.

Kaminski, T., Rayner, P. J., Heimann, M., and Enting, I. G.: On aggregation errors in atmospheric transport inversions, J. Geophys. Res., 106, 4703-4715, doi: 10.1029/2000JD900581, 2001.

MeteoSwiss: Klimabulletin Winter 2017/18, MeteoSwiss, Zurich, Switzerland, 2018.

Meteotest: Lachgas-Emissionskataster Schweiz, Aufbereitung von Datengrundlagen, Berechnung des Katasters, Meteotest, 40, 2017.

Michalak, A. M., Hirsch, A., Bruhwiler, L., Gurney, K. R., Peters, W., and Tans, P. P.: Maximum likelihood estimation of covariance parameters for Bayesian atmospheric trace gas surface flux inversions, J. Geophys. Res., 110, D24107, doi: 10.1029/2005JD005970, 2005.

Mittelbach, H.: Soil moisture in Switzerland. analyses from the Swiss soil moisture experiment, ETH, 2011.

Mittelbach, H., and Seneviratne, S. I.: A new perspective on the spatio-temporal variability of soil moisture: temporal dynamics versus time-invariant contributions, Hydrol. Earth Syst. Sci., 16, 2169-2179, doi: 10.5194/hess-16-2169-2012, 2012.

Myhre, G., Shindell, D., Bréon, F.-M., Collins, W., Fuglestvedt, J., Huang, J., Koch, D., Lamarque, J.-F., et al.: Anthropogenic and Natural Radiative Forcing, in: Climate Change 2013: The Physical Science Basis. Contribution of Working Group I to the Fifth Assessment Report of the Intergovernmental Panel on Climate Change, edited by: Stocker, T. F., Qin, D., Plattner, G.-K., Tignor, M., Allen, S. K., Boschung, J., Nauels, A., Xia, Y., Bex, V., and Midgley, P. M., Cambridge University Press, Cambridge, United Kingdom and New York, NY, USA, 659–740, 2013.

Olivier, J., and Janssens-Maenhout, G.: CO2 Emissions from Fuel Combustion - 2012 Edition, IEA CO2 report 2012, Part III, Greenhouse-Gas Emissions, ISBN 978-92-64-17475-7, 2012.

Oney, B., Henne, S., Gruber, N., Leuenberger, M., Bamberger, I., Eugster, W., and Brunner, D.: The CarboCount CH sites: characterization of a dense greenhouse gas observation network, Atmos. Chem. Phys., 15, 11147-11164, doi: 10.5194/acp-15-11147-2015, 2015.

Ravishankara, A. R., Daniel, J. S., and Portmann, R. W.: Nitrous Oxide (N_2O): The Dominant Ozone-Depleting Substance Emitted in the 21st Century, Science, 326, 123-125, doi: 10.1126/science.1176985, 2009.

Reay, D. S., Davidson, E. A., Smith, K. A., Smith, P., Melillo, J. M., Dentener, F., and Crutzen, P. J.: Global agriculture and nitrous oxide emissions, Nature Climate Change, 2, 410, doi: 10.1038/nclimate1458, 2012.

Rodgers, C. D.: Inverse Methods for Atmospheric Sounding, Series on Atmospheric, Oceanic and Planetary Physics, WORLD SCIENTIFIC C1 - Theory and Practice, 256 pp., 2000.

Ruckstuhl, A. F., Henne, S., Reimann, S., Steinbacher, M., Vollmer, M. K., O'Doherty, S., Buchmann, B., and Hueglin, C.: Robust extraction of baseline signal of atmospheric trace species using local regression, Atmos. Meas. Tech., 5, 2613-2624, doi: 10.5194/amt-5-2613-2012, 2012.

Stohl, A., Seibert, P., Arduini, J., Eckhardt, S., Fraser, P., Greally, B. R., Lunder, C., Maione, M., et al.: An analytical inversion method for determining regional and global emissions of greenhouse gases: Sensitivity studies and application to halocarbons, Atmos. Chem. Phys., 9, 1597-1620, doi: 10.5194/acp-9-1597-2009, 2009.

Taylor, K. E.: Summarizing multiple aspects of model performance in a single diagram., J. Geophys. Res., 106, 7183-7192, doi: 10.1029/2000JD900719, 2001.

Thompson, R. L., Ishijima, K., Saikawa, E., Corazza, M., Karstens, U., Patra, P. K., Bergamaschi, P., Chevallier, F., et al.: TransCom N_2O model inter-comparison – Part 2: Atmospheric inversion estimates of N_2O emissions, Atmos. Chem. Phys., 14, 6177-6194, doi: 10.5194/acp-14-6177-2014, 2014.

Glossary

BRM	Beromünster tall tower observatory.
CRDS	**C**avity **R**ing **D**own **S**pektrometer.
COSMO	**CO**nsortium for **S**mall scale **MO**delling: The operational numerical weather prediction model of MeteoSwiss.
COSMO7	Operational COSMO run by MeteoSwiss providing meteorological analysis fields for the European domain with a horizontal resolution of 7 km x 7 km.
ECMWF	**E**uropean **C**entre for **M**edium-Range **W**eather **F**orecasts.
EMEP	**E**uropean **M**onitoring and **E**valuation **P**rogramme.
FLEXPART	Langrangian Particle Dispersion Model driven by ECMWF model output.
FLEXPART-COSMO	Langrangian Particle Dispersion Model driven by COSMO model output.
GAW	**G**lobal **A**tmosphere **W**atch.
IPCC	**I**nternational **P**anel for **C**limate **C**hange.
JFJ	**J**ung**f**rau**j**och high-altitude observatory.
LPDM	**L**angrangian **P**article **D**ispersion **M**odel. Describe a class of atmospheric numerical models that simulate the transport and dispersion of trace compounds by solving the trajectory equation for a large number of air particles (parcels) that undergo mean and turbulent (stochastic process) transport.
NIR	**N**ational **I**nventory **R**eporting of greenhouse gas emissions.
NOAA	**N**ational **O**ceanic and **A**tmospheric **A**dministration.
NOAA ESRL GMD	NOAA, **E**arth **S**ystem **R**esearch **L**aboratory, **G**lobal **M**onitoring **D**ivsion
NWP	**N**umerical **W**eather **P**rediction.
ppb	**p**arts **p**er **b**illion per volume. Number of molecules of a target gas 10^9 molecules of air (volume mixing ratio or also mole fraction). The atmospheric composition of trace gases is usually given as dry air mole fractions, hence, referring to the number of air molecules expect for water vapour molecules. 1 ppb = 1 nmol mol^{-1}.
ppm	**p**arts **p**er **m**illion per volume. Same as for ppbv, but 3 orders of magnitude larger (number of molecules per 10^6 molecules of (dry) air). 1 ppm = 1 µmol mol^{-1}.
REBS	**R**obust **E**stimation of **B**aseline **S**ignal
RMSE	**R**oot **M**ean **S**quare **E**rror.
SSL	**S**chauin**sl**and observatory, UBA, Germany.
UBA	**U**mwelt**b**undes**a**mt, German environmental protection agency.
UNFCCC	**U**nited **N**ations **F**ramework **C**onvention on **C**limate **C**hange.
WCC	**W**orld **C**alibration **C**enter (part of WMO GAW).
WMO	**W**orld **M**eteorological **O**rganization.